University of Cape Town

The Effect of δ Rays on Impact Parameter Resolution in Pixel Detectors

by

Angus Comrie

A dissertation submitted for the
degree of Master of Science

in the
Faculty of Science
Department of Physics

May 2011

Plagiarism Declaration

I know the meaning of plagiarism and declare that all of the work in the following dissertation, save for that which is properly acknowledged, is my own.

_____

Angus Comrie

University of Cape Town

Abstract

Faculty of Science
Department of Physics

MSc Thesis

by Angus Comrie

A review of the ALICE detector in the context of heavy ion collisions is given, along with a discussion on the use of Monte Carlo simulations in high energy physics. An investigation of the accuracy of GEANT3 simulation of low energy electrons is detailed. It shows that, below kinetic energies of 1 MeV, GEANT3 simulation of the passage of electrons across medium boundaries does not match experimental data. In the main part of the thesis, the effect of δ rays (secondary ionising electrons) originating in the beam pipe and inner layers of the Inner Tracking System (ITS) pixel detector on the impact parameter resolution is investigated, again via Monte Carlo simulation. A comparison between the impact parameter resolution of the current ITS geometry and a proposed upgrade, in which the pixel size is reduced and the layer radii are decreased, is given. It is shown that, while the upgraded geometry has an improved resolution, the effect of δ rays is exaggerated.

Acknowledgements

Over the course of my degree, I have received help from many sources, both inspirational and constructive. Thanks to Dr. Bruce Becker, for getting me started on ROOT and GEANT simulations; to Prof. Jean Cleymans, for sparking my interest in particle physics and for giving me the freedom to work with people from all over the world; to Dr. Emanuele Quercigh, for his tireless support and suggestions on the direction of my work; to Dr. Spencer Wheaton, for all the help with writing up what would otherwise be a convoluted and poorly edited dissertation.

Contents

Chapter 1

Introduction

The study of high energy particle collisions is presently the best method for investigating the behaviour of matter under extreme conditions, such as high temperatures or energy densities. High energy densities can be obtained by accelerating and subsequently colliding heavy ions such as lead or gold. At sufficiently high densities, hadronic matter undergoes a phase change from baryonic or mesonic to a state in which the individual quarks and gluons may become deconfined, a state for which hadronic degrees of freedom do not provide a sufficient description. This may have been observed in recent experiments at the Relativistic Heavy Ion Collider (RHIC) [1]. The deconfined state is known as the quark-gluon plasma (QGP).

Charm and Beauty quarks are abundantly produced in the QGP as primary products of heavy ion collisions. These heavy quarks emerge as hadrons, such as the D^0 meson, as the medium cools to a hadronic state. The production rates of these hadrons depend heavily on the conditions just after the collision. Thus, studying their production and kinematics can reveal information about the deconfined medium itself. However, charm and beauty hadrons decay via the weak interaction with a mean path in the order of 100 μm [2], making their direct detection infeasible. Instead, their decay vertices must be determined by tracking secondary decay products. Differentiating between the primary and secondary decay vertices requires an excellent resolution on the impact parameter of a track, defined as the distance of closest approach from the track to the primary collision vertex.

In the ALICE (A Large Ion Collider Experiment) detector at the Large Hadron Collider (LHC), the Inner Tracking System (ITS) is largely responsible for the

resolving of the decay vertices, with the two innermost layers playing the most vital role. These layers consist of Silicon Pixel Detectors (SPDs) arranged in a cylindrical geometry coaxial with the beam pipe. This study examines the effect of energetic ionising electrons, produced by ionising decay products such as pions, on the SPD's impact parameter resolution. These energetic electrons, or δ rays, may trigger signals in pixels erroneously, leading to a poor impact parameter resolution. In view of a proposed upgrade to the ITS, this study examines the improvements in impact parameter resolution that may be obtained by modifying the SPD geometry. It is speculated that a decrease in individual pixel size and the placing of the innermost SPD layer against the beam pipe will result in an improved impact parameter resolution, but that the effects of δ rays will become more detrimental in this new arrangement. In order to determine the effect of δ rays on impact parameter resolution, a Monte-Carlo simulation of pions travelling through a simple pixel detector, modelled on the ITS pixel detectors, was performed using the particle transport package GEANT3.

Chapter 2 gives an overview of the physics of heavy ion collisions and discusses a few possible signatures of the quark-gluon plasma, as well as the results from RHIC. Chapter 3 describes the ALICE detector and details the ITS and the interactions of charged particles with the SPDs. Chapter 4 discusses the process of Monte-Carlo simulation, describes the process of particle transport in Monte-Carlo simulations and presents verification of the behaviour of δ rays in GEANT3. Chapter 5 discusses the simulation of a simple pixel detector and the analysis of results. Concluding remarks are made in Chapter 6. A brief discussion on variables and quantities of interest in high energy physics is given in Appendix A.

Chapter 2

Overview of Heavy Ion Physics

2.1 Heavy Ion Collisions

The interactions between elementary quarks and the gluons that carry the strong force are described by the theory of Quantum Chromodynamics (QCD). At sufficiently high pressure and temperature, hadronic matter is expected to undergo a phase transition to a state of matter in which the constituent quarks become deconfined, forming a plasma of "free" quarks and gluons [3]. The underlying process for this deconfinement is similar to the phenomenon of Debye screening in electrodynamics, whereby a cloud of electric charge causes the effect of a single charge to be reduced. The same phenomenon can be applied to the colour charges of quarks in a dense medium. At a point where the Debye radius r_D[1] is smaller than the hadronic binding radius, strong forces are no longer able to confine a hadron's constituent quarks and they effectively become free [4]. Lattice-based QCD simulations predict that the phase transition occurs at a temperature in the region of 200 MeV [5] at zero baryon chemical potential μ_B (i.e. zero net baryon density), or an energy density in the region of 1 GeV/fm^3. QCD predicts a phase diagram for matter in the plane of temperature versus μ_B, shown in Figure 2.1, which consists of three distinct phases of matter: hadronic at low T and μ_B, quarkyonic at larger values of μ_B and quark-gluon plasma (QGP) at high temperature and low μ_B. The three phases co-exist only at the triple point of the phase diagram, estimated to be in the region of $\mu_B \approx 400$ MeV and $T \approx 150$ MeV [6].

[1] r_D is defined as the distance at which the force is screened by a factor of $1/e$.

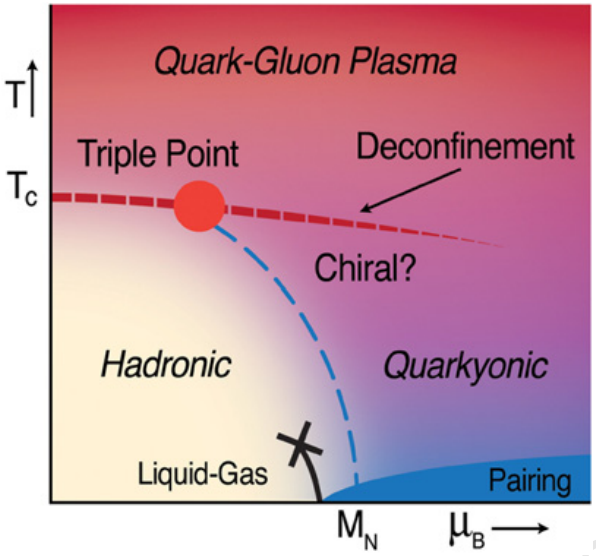

FIGURE 2.1: Phase diagram predicted by QCD calculations. Heavy ion collisions at high energies come close to $\mu_B = 0$ at high temperature, which are the conditions believed to have been active during the early universe, before hadronization. The transition to QGP is expected for temperatures above T_C, while a transition to the quarkyonic state of matter is expected at low temperatures for values of μ_B larger than the nucleon mass M_N [6].

In order to reach the high energy densities required to allow the creation of the quark gluon plasma, heavy ions can be collided at ultra-relativistic energies, in which head-on collisions leave an enormous amount of energy for the creation of elementary particles in a concentrated region. At ultra-relativistic speeds, the colliding ions are Lorentz contracted along the beam axis (z-axis) by a factor of $\gamma = E/m$. At energies of the Large Hadron Collider (LHC), $\gamma \approx 2800$ for heavy ions [7], substantially reducing the region in which collisions between individual nucleons occur and thus increasing the energy density in this region. At such high energies, a large number of quark-antiquark pairs are created, of zero net baryon number, far outweighing the initial baryon numbers of the colliding nuclei. This requires the baryon chemical potential μ_B to be almost zero, which corresponds to the conditions of the early universe, of extremely high temperatures and approximately equal amounts of quarks and antiquarks. Thus, the study of heavy ion collisions and the possible creation of the QGP gives insight into the first microseconds after the big bang and into the process of hadronization. The interpenetration time, defined as the time from the initial overlap of nuclei to the coincidence of their centres, is given by $\tau_0 = 2R/\gamma$. At high energies, this time is shorter than the time for initial parton showers to form, enabling the system to be described by a hydrodynamical model before hadronization and "freeze-out" occurs [3]. Chemical

freeze-out, after which hadron yields are fixed, occurs shortly after hadronization, at the chemical freeze-out temperature T_{ch}. The fixing of the thermal distributions, or thermal freeze-out, occurs at the freeze-out temperature T_{fo}. The evolution of a heavy ion collision in space-time is shown in Figure 2.2. The time taken for gluons to thermalize is significantly lower than that taken by quarks. Thus, during the first phase of the QGP one could expect gluon domination [8].

Due to the nature and lifetime of the QGP one cannot directly observe it. Rather, one can infer its existence and properties from particles produced inside the medium. The conditions under which particle production occurs, as well as the properties of the medium through which created particles travel, have a significant effect on the yields measured by detectors, as well as their kinematic properties. A few of the significant postulated signatures of QGP production are described in detail in Section 2.2.

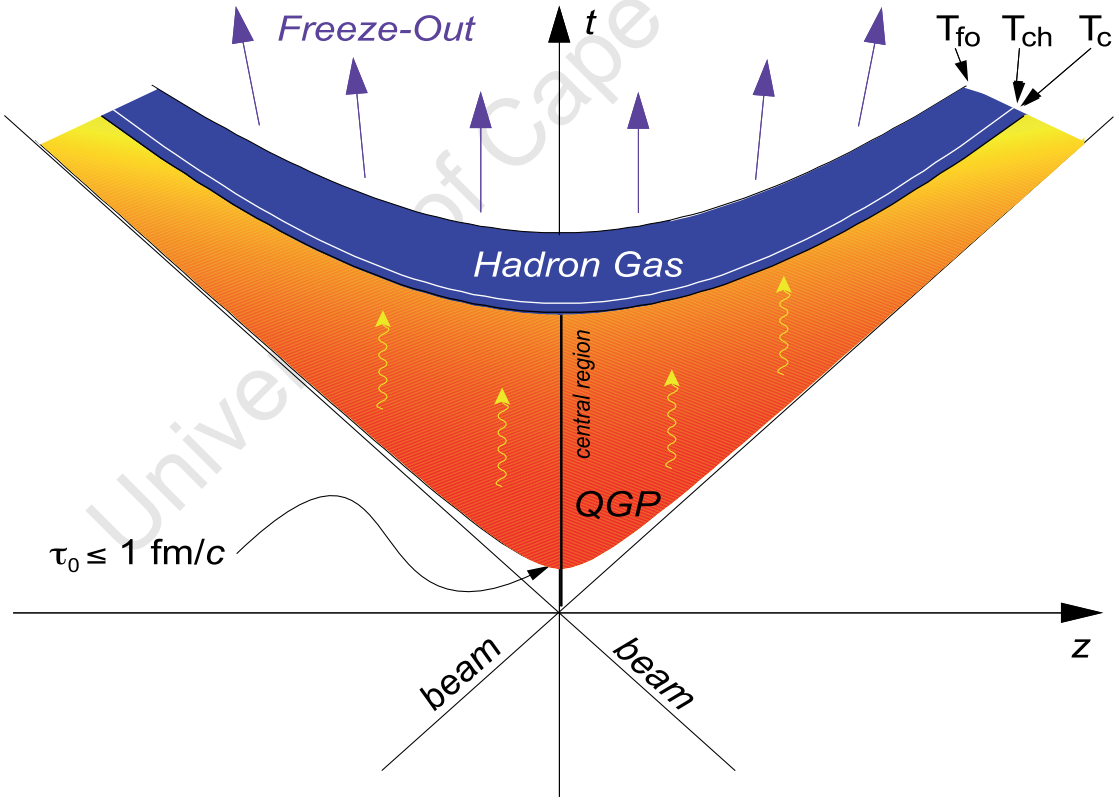

FIGURE 2.2: Space-time evolution of a heavy ion collision. The system cools as it expands towards hadronization, chemical freeze-out and finally thermal freeze-out [9].

2.2 Selected Observables of Heavy Ion Collisions Capable of Signalling QGP Production

2.2.1 Suppression of Heavy Quarkonia Production in a QGP

Quarkonium is the bound state of a quark and its antiquark. Quarkonia such as J/ψ ($\mathbf{c\bar{c}}$) and Υ ($\mathbf{b\bar{b}}$) are produced primarily from hard parton interactions [4]. An initial quark-antiquark pair is produced, followed by resonant interaction which creates the bound quarkonium state. However, if the quark-antiquark pair is produced in a deconfined medium such as the quark gluon plasma, the formation of the quarkonium state could be prevented if the Debye screening radius (discussed in Section 2.1) is smaller than the binding radius of the quarkonium. As the screening radius decreases with increasing temperature, this will occur when the temperature of the formed QGP is sufficiently high. As an example, a non-relativistic interaction potential for the $\mathbf{c\bar{c}}$ system is given by

$$V(r,T) = \sigma(T)r - \frac{\alpha}{r}, \tag{2.1}$$

with $\sigma(T)$ as the string tension and α as the effective coulombic interaction coupling constant [4]. At high temperatures, σ decreases and, at deconfinement, $\sigma = 0$. Thus, at temperatures higher than the deconfinement temperature T_c, the interaction will be given by

$$V(r,T) = -\frac{\alpha}{r}\exp\left(\frac{-r}{r_D}\right), \tag{2.2}$$

where the modification to the surviving term of Equation 2.1 is due to the Debye colour screening. The total energy of the system is given as

$$E(r,T) = 2m + \frac{m}{2r^2} + V(r,T), \tag{2.3}$$

where m is the mass of the charm quark. Minimising the total energy gives

$$\frac{r}{r_D}\left(\frac{r}{r_D}+1\right)\exp\left(-\frac{r}{r_D}\right) = (m\ \alpha\ r_D)^{-1}. \tag{2.4}$$

The left-hand-side has a maximum of 0.84 at $r/r_D = 1.61$ and thus a solution exists only if $(m\alpha r_D)^{-1} \leq 0.84$ [4]. Hence, the smallest screening radius allowing a bound charmonium state is

$$r_D^{\min} = \frac{1}{0.84\ m\alpha}. \tag{2.5}$$

Lattice QCD calculations at $T/T_c = 1.5$ give $\alpha \approx 0.2$, which gives $r_D^{\min} = 0.76$ fm [10]. An upper bound of r_D is given by the quark-antiquark correlation length $\xi(T)$ [4], which drops to approximately 0.2 fm at $T/T_c = 1.5$, well below $r_D^{\min}$. Thus, the J/ψ bound state cannot form at sufficiently high temperature and instead the charm quark pair will split and travel through the medium, eventually forming "open" charm pairs such as $\mathbf{c\bar{u}}$ or $\mathbf{\bar{c}u}$. However, this prohibition is not complete: In the peripheral region of the deconfinement medium, formation will still occur. Thus, the yield of heavy quarkonia will be merely suppressed rather than absent. Heavy quarkonia yields can be measured by their decay into a muon pair with unlike signs:

$$J/\psi \rightarrow \mu^+\mu^-.$$

The invariant mass of the parent particle can be determined from the energy of the measured muon pair.

2.2.2 Suppression of High-p_T Particles

Particles with high transverse momentum[2] p_T are the result of parton-parton interaction [11]: hard parton-parton interactions give rise to high-p_T back-to-back quark-antiquark pairs which then hadronize into jets of high-p_T mesons. One can measure these jets and experimental results show that a back-to-back correlation of high-p_T particles exists [12]. It is predicted that high energy particles inside a deconfined medium will experience energy loss via "gluonic bremmstralung" in which high energy particles will interact with the medium and radiate energy, proportional to the square of the distance travelled through the medium [11]. This will result in a suppression of the high-p_T spectra. If, in addition, jet production occurs in the peripheral region of the deconfined medium, the back-to-back correlation will be suppressed as one jet may have travelled significantly further than the other and may have effectively been "quenched" by the medium. One can

[2]Kinematic variables such as p_T are discussed in Appendix A.1

detect high-p_T suppression by measuring the nuclear modification factor R_{AA}, defined in Appendix A.2, for mesons with high (≥ 2 GeV/c) momenta. To measure the correlation of back-to-back jets and the suppression thereof, one can select measured events with a high-p_T meson present and then examine the azimuthal distribution of high-p_T particles within the same event [13]. The result for unsuppressed correlation will be peaks at $\phi = 0$ (due to particles arising from the same jet as the trigger particle) and at $\phi = \pi$ (due to particles arising from the jet opposite to that of the trigger particle), where ϕ is the azimuthal angle relative to the triggering high-p_T meson. For suppressed correlation, a less noticeable peak at $\phi = \pi$ is expected, due to jet quenching.

2.2.3 Heavy Quark Decay Vertices

At LHC energies, heavy ion collisions produce heavy quarks in abundance. One topic of interest is the comparison between quenching of heavy and light quarks in the production medium. As free quarks cannot exist outside the QGP, the production of charmed and bottom mesons such as D^0, as well as quarkonia such as J/ψ, are the only signs of heavy quark pair production in the QGP. The $D^0 \to K^-\pi^+$ and $D^+ \to K^-\pi^+\pi^+$ decay channels are two of the most well-understood channels for charm detection [14]. Both the D^0 and D^+ mesons decay via the weak interaction, with a mean proper decay length of $c\tau = 120$ μm and $c\tau = 310$ μm respectively [2]. The decay of these mesons will therefore result in a secondary decay vertex a small distance from the primary collision vertex. The identification of these secondary vertices requires a detector with excellent vertex position resolution. A schematic representation of the $D^0 \to K^-\pi^+$ decay, including the impact parameters[3] of the decay products, is shown in Figure 2.3.

2.3 Results from RHIC

Many of the topics addressed by the ALICE experiment at the LHC build on work done by RHIC at Brookhaven National Laboratory. Results from collisions at energies up to 200 GeV/u at RHIC contributed greatly to the understanding of heavy ion physics, but left many questions unanswered. While not being able to

[3]Impact parameter and other measured quantities are discussed in Appendix A.2.

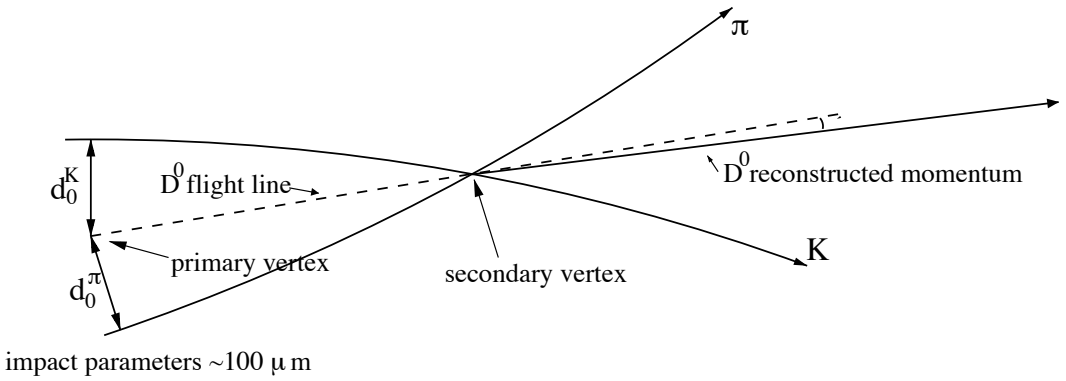

FIGURE 2.3: Schematic representation of $D^0 \to K^-\pi^+$ or $\overline{D^0} \to K^+\pi^-$ decay in the presence of an applied magnetic field, causing charged tracks to bend. The pion and kaon emerge from the secondary vertex, which can be reconstructed from the intersection of the two tracks [15].

conclusively answer the question "Was a quark gluon plasma formed?", analysis of events at RHIC show that an extremely dense medium was formed for which descriptions based purely on hadronic degrees of freedom were insufficient [13] and some of the expected signatures of QGP were observed. The most striking of all was the measurement of a suppression by a factor of up to 5 of the nuclear modification factor R_{AA} in the emission of high-p_T charged hadrons in central collisions, shown in Figures 2.4 and 2.5, which was not observed in d+Au collisions (Figure 2.6), as well as a suppression of away-jets as measured by the angular distribution of particles within high-p_T events, shown in Figure 2.7. However, many phenomena expected to be present in QGP, such as the extended lifetime predicted from hydrodynamic models [1], the restoration of chiral symmetry and the suppression of heavy quarkonia such as J/ψ were not observed [13]. Furthermore, the elliptic flow of mid-rapidity particles was not in line with hydrodynamic predictions [13], shown in Figure 2.8. The nature of the medium formed was concluded to be unlike the ideal gas based model of a QGP that had been predicted for very high temperatures. Instead, the medium displayed fluid-like properties with significant interaction, possibly a strongly-interacting quark gluon plasma (sQGP) [12].

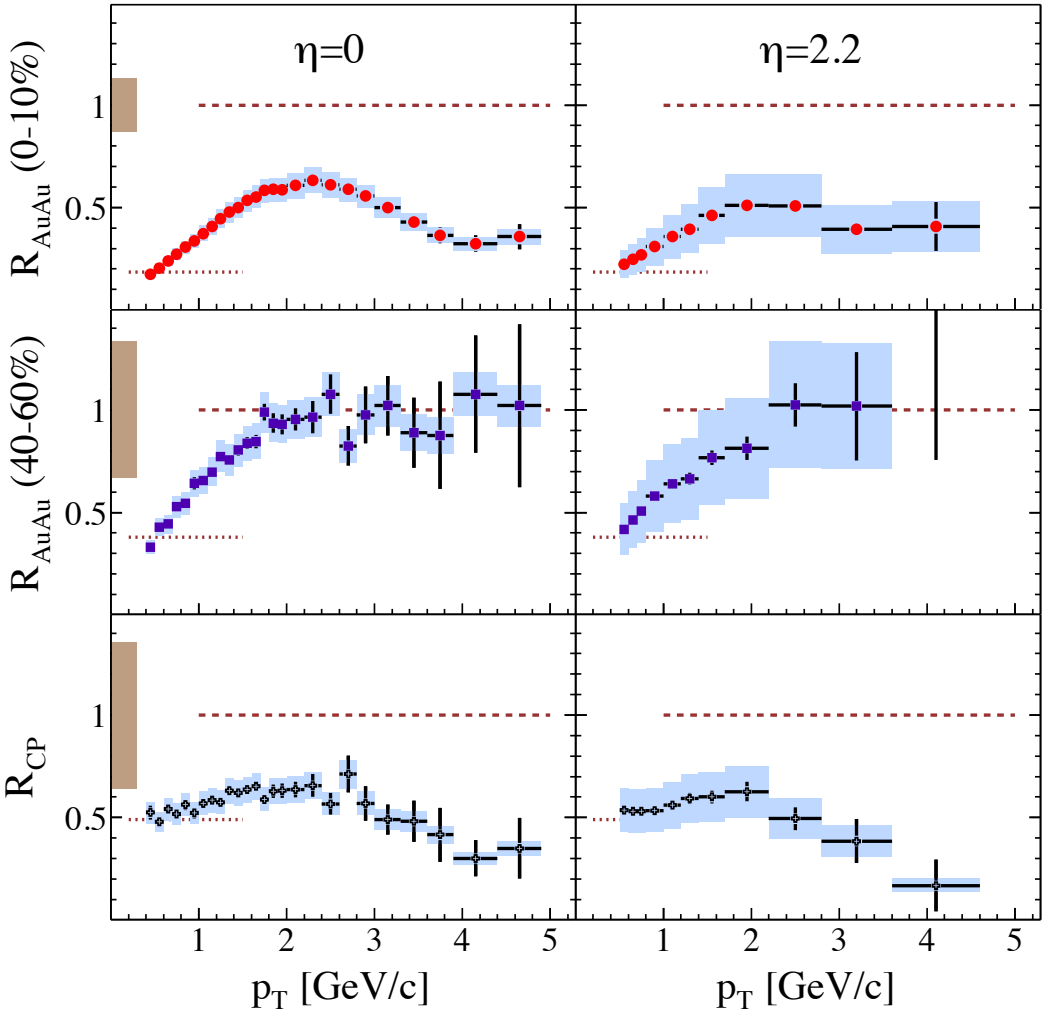

FIGURE 2.4: Nuclear modification factor R_{AA} for charged hadrons, as measured by the BRAHMS detector at RHIC [1]. R_{AA} is shown for central collisions (0-10%) as well as for semi-peripheral collisions (40-60%). The ratio between the two, R_{CP}, is also shown. There is a suppression of R_{AA} in central collisions, especially at high p_T.

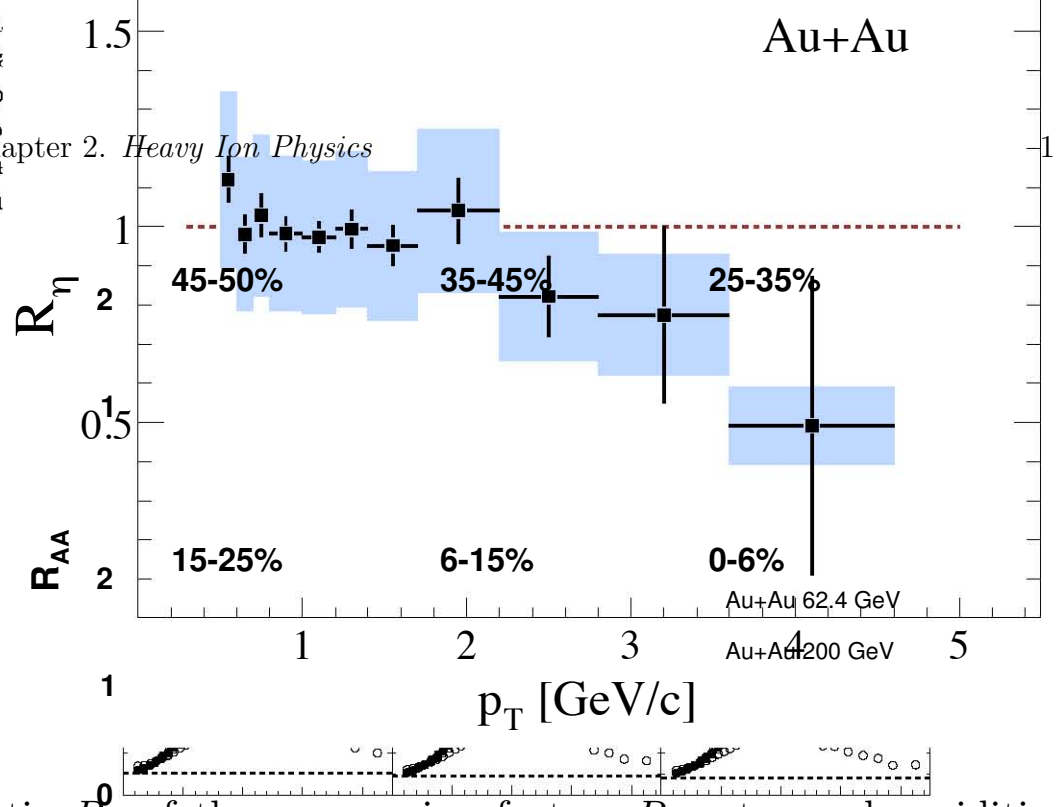

Fig. 12. Ratio R_η of the suppression factors R_{cp} at pseudorapidities $\eta = 0$ and $\eta = 2.2$ that are shown in figure 11. The figure suggest that high p_T suppression persists (and is even more important) at forward rapidity than at $\eta = 0$ [48].

may come into play at forward rapidities (see discussion on the Color Glass Condensate in the following chapter).

FIGURE 2.5: Nuclear modification factor, R_{AA}, as a function of transverse momentum for Au+Au collisions at $\sqrt{s_{NN}} = 62.4$ (closed symbols) and 200 GeV (open symbols), for different centrality ranges [13]. Error bars represent statistical uncertainties only, while boxes around unity represent systematic uncertainties in the total inelastic cross section. A suppression of high p_T occurs in 200 GeV collisions.

Fig. 8: Nuclear modification factor, R_{AA}, as a function of transverse momentum for Au+Au collisions at $\sqrt{s_{NN}} = 62.4$ (closed symbols) and 200 GeV (open symbols), for different centrality ranges [13]. Error bars represent statistical uncertainties only, while boxes around unity represent systematic uncertainties in the total inelastic cross section. A suppression of high p_T occurs in 200 GeV collisions. One can see that a smaller suppression is observed in 62.4 GeV collisions. Errors shown are statistical and systematic uncertainties, respectively. The grey bands show the systematic error in the overall scale due to N_{coll}. The solid (dashed) line shows the expect

Appendix

The PHO

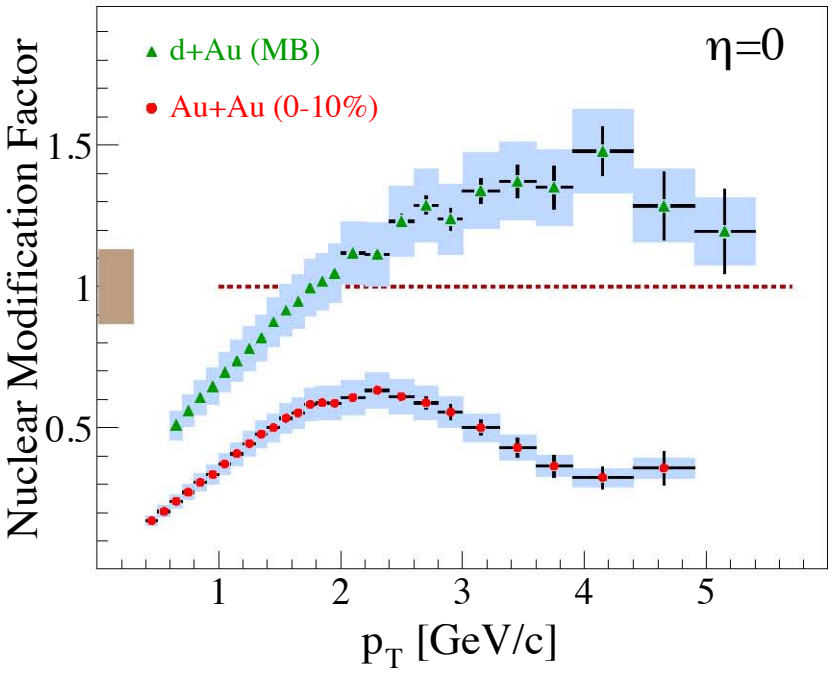

Fig. 13. Nuclear modification factors measured for central Au+Au collisions and minimum bias d+Au collisions at $\sqrt{s_{NN}} = 200$ GeV, evidencing the important high p_T suppression observed in central Au+Au collisions [48] which is absent in the d+Au reactions. The shaded band around the points indicates the systematic errors. The shaded box on the ordinate around unity shows the estimated uncertainty on the value of N_{bin}.

FIGURE 2.6: Nuclear modification factor for charged hadrons in d+Au collisions and central Au + Au collisions, as measured by the BRAHMS detector at RHIC [1]. The graph shows that there is a significant suppression at high p_T for central Au+Au collisions that is not replicated in d+Au collisions. This may be because the energy density in d+Au collisions is not sufficient to form a QGP.

It has been conjectured that the observed high p_T suppression might be the re

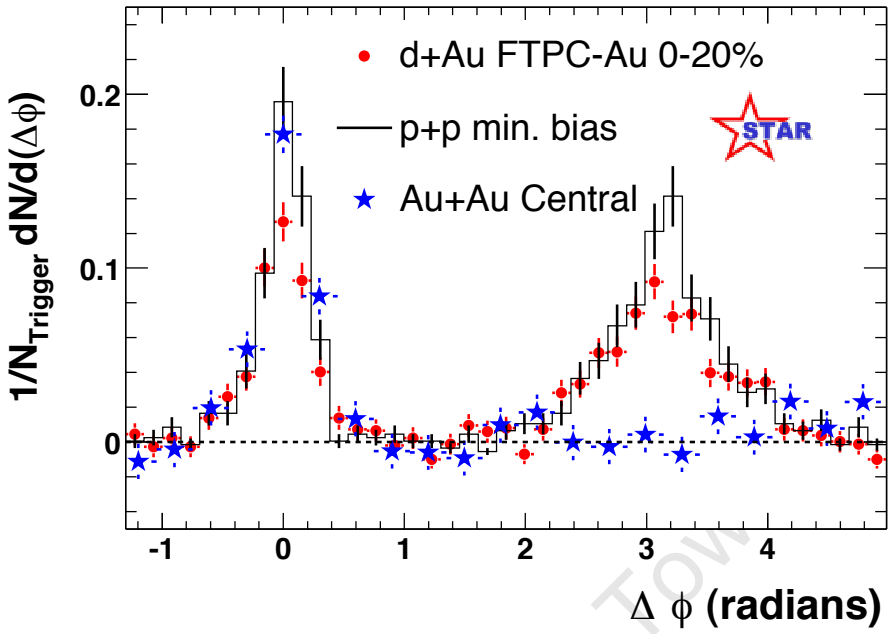

FIGURE 2.7: Differential yields per $\Delta\phi$ and per trigger particle for hadron pairs in central Au+Au collisions, as well as d+Au collisions, measured by the STAR detector at RHIC [12]. There is a noticeable difference in the size of the peaks for trigger jets ($\Delta\phi \approx 0$) and peaks for away-side jets ($\Delta\phi \approx \pi$) for central Au+Au collisions.

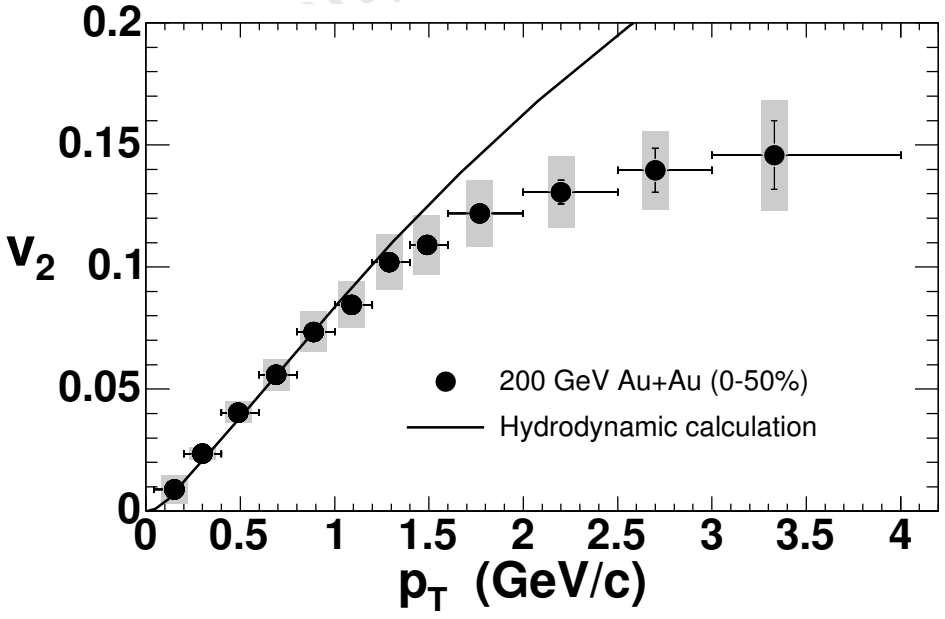

FIGURE 2.8: Elliptic flow of mid-rapidity charged particles in central Au+Au collisions, measured by PHOBOS [13]. At higher p_T, there is a significant deviation from the relativistic hydrodynamics prediction.

Chapter 3

The ALICE Detector

3.1 Overview of the ALICE Detector

The LHC at CERN, shown schematically in Figure 3.1, is a high energy particle accelerator, designed to collide protons or heavy ions that have been accelerated to energies of up to 7 TeV per participant in the case of proton-proton collisions, and 2.76 TeV/u in the case of Pb-Pb collisions. Acceleration up to full energy is staged via the use of linear accelerators initially: LINAC 2 produces a 50 MeV proton beam, while LINAC 3 produces a beam of Pb ions of energy 4.2 MeV/u [16]. Both are then accelerated through the Proton Synchrotron (PS) and Super Proton Synchrotron (SPS) before being fed into the main LHC ring. This ring, which is 27 km in circumference, consists of two beam pipes that intersect at four points, at which five detectors are placed: ATLAS, ALICE and LHCb are each positioned at individual intersection points, while CMS and TOTEM share an intersection point. Two other detectors, for use in the LHCf experiment, are positioned 140 m on either side of an intersection point.

While detectors such as ATLAS and CMS are designed to measure a wide range of physical processes for both heavy ion and proton collisions, the ALICE detector is designed primarily to measure particles produced in heavy ion collisions at ultra-relativistic energies, and is built to handle charged particle multiplicities of approximately $dN_{\mathrm{ch}}/d\eta = 8000$ at mid-rapidity [17]. It is tasked with measuring the nature of strongly-interacting matter and exploring the existence of the quark gluon plasma (QGP) [18]. The ALICE detector is made up of various sub-detectors, shown in Figure 3.2:

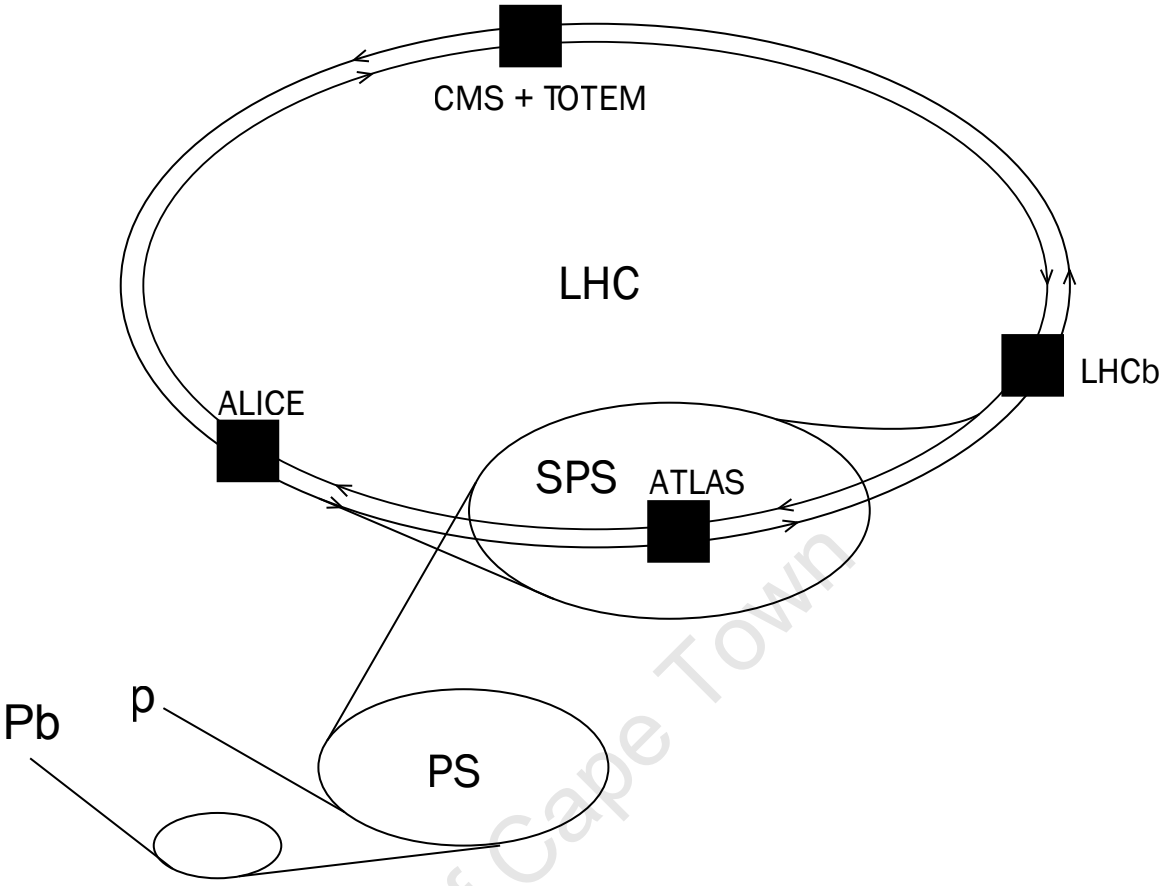

FIGURE 3.1: Schematic view of the LHC. Both proton and lead sources are accelerated initially through a LINAC before feeding into the PS, SPS and finally LHC. 4.2 MeV/u lead ions are placed in the Low-Energy Ion Ring (LEIR) for storage and cooling.

- **Inner Tracking System (ITS)**: The ITS is made up of six cylindrical silicon detector layers that lie coaxial to the beam pipe, with radii ranging from 3.9 cm to 43.0 cm [19]. The outermost layer is used to match tracks with the Time-Projection Chamber (TPC) [17]. ITS provides low momentum track finding and high resolution (<100 μm) impact-parameter localization [19].

- **Time-Projection Chamber (TPC)**: The primary central detector of ALICE, the TPC, is a cylindrical field cage filled with $Ne/CO_2/N_2$ drift gas under a high voltage gradient. It has an inner radius of 85 cm and an outer radius of 250 cm, sandwiched between cathode pads. Like the ITS, the TPC's pseudo-rapidity acceptance range is $|\eta| < 0.9$ [19]. It provides efficient tracking of charged particles with $p_T > 150$ MeV/c and, for the purpose of Hanbury Brown and Twiss interferometry, high resolution two-track measurements:

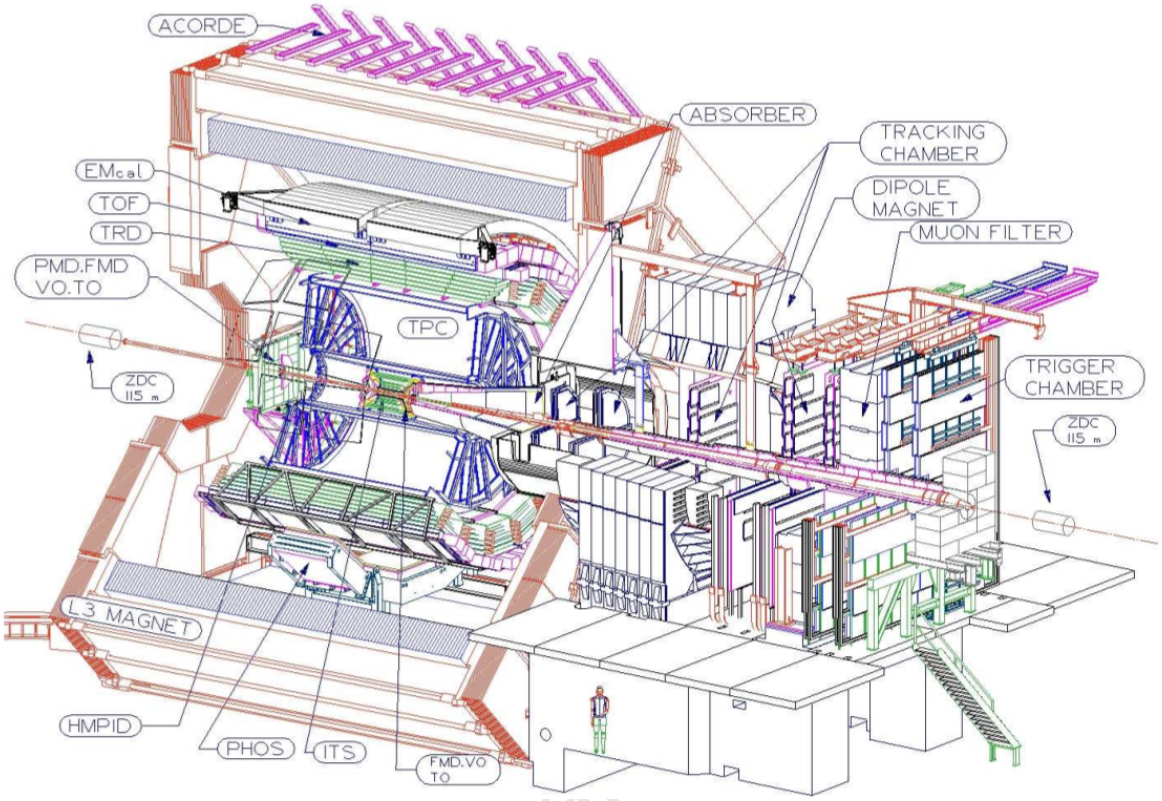

FIGURE 3.2: The ALICE detector. The various sub-detectors as well as an outline of the muon arm are shown [19].

The resolution of the relative momentum between tracks is less than 5 MeV/c [19].

- **Transition-Radiation Detector (TRD)**: The TRD provides identification of mid-rapidity electrons with momenta greater than 1 GeV/c via six layers of cathode pads (arranged coaxially to the other central detectors) whose radii vary from 290 cm to 368 cm [20]. It enhances the tracking capabilities of the TPC and improves the position and momentum resolution. The TPC also measures the specific energy loss of pions and electrons with $p_T \sim 2$ GeV/c and acts as a trigger for high-p_T events, improving detection of Υ states and recognition of jet production [19].

- **Time-Of-Flight Detector (TOF)**: The TOF detector provides identification of pions, kaons and protons in the intermediate momentum range, as well as detection of open heavy-flavoured states and vector-meson resonances [19]. It consists of Multi-gap Resistive-Plate Chambers (MRPCs) placed coaxially around the TPC. The TOF detector has a total of 150 000

readout channels [21]. With a pseudo-rapidity range of $|\eta| < 0.9$, it is designed to conform to the geometry of the inner detectors, minimising the dead zones of the central detectors as a whole [17].

- **High-Momentum Particle Identification Detector (HMPID)**: The HMPID provides identification of particles with transverse momentum in the GeV/c range, as well as the identification of light nuclei and anti-nuclei with high p_T [19]. The pseudo-rapidity range covered is $|\eta| < 0.6$. It comprises of seven Ring Imaging Cherenkov counters containing a layer of C_6F_{14} liquid, in which charged particles emit a Cherenkov radiation cone, which is detected by a photon counter.

- **PHOton Spectrometer (PHOS)**: PHOS detects low-p_T photons, high-p_T π^0's and η mesons in a highly central rapidity range ($|\eta| < 0.12$) via a high-resolution electromagnetic calorimeter, placed 460 cm below the interaction point [22]. It will allow the inference of thermal and dynamical properties of the initial collision phase, such as the temperature, via direct photon measurements, as well as a study of jet quenching from measurements of high-p_T π^0's [19].

- **ElectroMagnetic Calorimeter (EMCal)**: EMCal is a large cylindrical calorimeter, consisting of lead scintillators, with a radius of approximately 450 cm. It provides measurements of jet quenching from measurements of high-p_T particles. It covers the central pseudo-rapidity range of $|\eta| < 0.7$ [19].

- **ALICE COsmic Ray DEtector (ACORDE)**: ACORDE focuses on cosmic ray events, detecting atmospheric muons and muon bundles via an array of plastic scintillator counters, placed at the very top of the ALICE experimental setup. ACORDE also serves as a trigger for the other detectors during calibration and alignment [19].

- **Forward muon spectrometer**: The forward muon spectrometer provides dedicated muon detection in the pseudo-rapidity range $-4 < \eta < -2.4$. The muon spectrometer measures the complete spectrum of the heavy quark resonances: J/ψ, ψ', Υ, Υ' and Υ'', via their decay into muon pairs of unlike signs. In addition, the dimuon continuum will be measured, up to invariant masses in the region of 10 GeV/c^2, where most muonic decays are expected to arise from open charm and beauty [19]. It consists of ten detection planes

placed at intervals in the region of a large bending magnet. A large front absorber limits the number of hadrons and photons passing through to the detectors.

- **Zero-Degree Calorimeters (ZDC):** The ZDC provides detection of spectator nucleons for centrality measurements and an estimate of the reaction plane, via two hadron calorimeters 116 m from the interaction point on either side.

- **Photon Multiplicity Detector (PMD):** The PMD gives multiplicity measurements in the pseudo-rapidity range of $2.3 < \eta < 3.7$, as well as estimations of the reaction plane, from over 4 000 gas proportional counter chambers, arranged in a honeycomb design.

- **Forward Multiplicity Detector (FMD):** The FMD provides charged particle multiplicity measurements on both sides of the interaction point, measuring in the rapidity range of $-3.4 < \eta < -1.7$ and $1.7 < \eta < 5.0$. The FMD is made up of 5 rings, each containing over 10 000 silicon sensor strips, placed coaxial to the beam line.

- **V0 Detector**: This detector provides charged particle multiplicity measurements on both sides of the interaction point via the signal amplitude of scintillator arrays, which provide a measure of centrality, as well as measurements of luminosity in proton collisions.

- **T0 Detector**: The T0 detector provides trigger signals, depending on the primary vertex position and start times for the TOF detector [19], via arrays of 12 Cherenkov counters on either side of the interaction point.

At maximum luminosity, event rates for heavy ion collisions at LHC are expected to be in the region of 8 kHz [19]. In order to bring that rate down to a feasible level for the data acquisition (DAQ) system, a trigger system is implemented, by which events possessing certain characteristics are accepted, while others are rejected. ALICE employs a hierarchical trigger system. L0 trigger signals are sent to the Central Trigger Processor (CTP) and forwarded to detectors within 1.2 μs. Additional trigger information follows in the L1 trigger signal at 6.5 μs, while a final L2 signal is sent after 88 μs that confirms that no additional central collisions have been captured, as this would lead to multiplicities above some detectors' capabilities [19]. In addition, a software-based trigger, the High Level Trigger

(HLT), can be employed which performs online analysis and event reconstruction via a cluster of PCs. The HLT can be used to determine whether events are stored by DAQ [19].

Owing to its relevance to the major focus of this work, the ITS will be discussed in more detail, with specific focus on the SPDs.

3.2 The Inner Tracking System (ITS)

At radii close to the beam pipe, extremely high track densities are expected (up to 90 cm^{-2} [23]). In order to cope with these track densities, highly granular detectors are required. The Inner Tracking System (ITS) is built with that in mind. Its primary functions are to determine primary and secondary decay vertices with a resolution of better than 100 μm, to identify and track low-momentum particles and to improve the momentum resolution of measurements made by the TPC [23]. The six cylindrical silicon detector layers are shown schematically in Figure 3.3. Two layers of each type (silicon pixel, silicon drift and silicon strip, each with a unique type of elementary detection unit, or "cell") are present in the ITS. Various parameters of each layer type are shown in Table 3.1. Charged particles travelling through the detectors are subject to collisions with the individual atoms that constitute the detector media and are thus subject to energy loss and scattering. The energy deposited in cells triggers a signal, from which parameters such as the position and (in the case of analogue detectors) the momentum of the ionising particle can be measured. The size of individual cells limits the spatial precision, defined as the mean deviation of the measured position from the exact position of the ionising particle passing through the cell[1].

The primary factors influencing the design of the ITS were [23]:

- **Rapidity Acceptance:** A large rapidity acceptance range is necessary in order to accurately study particle ratios, p_T spectra and the detection of low-p_T highly massive particles. This was chosen to be $|\eta| < 0.9$, with the inner pixel layer providing a range of $|\eta| < 1.98$.

[1] If the cell is only digital, one can approximate this deviation by assuming a uniform distribution of exact positions, while the measured position will always be given by the position of the centre of the pixel. Thus, the deviation in each dimension is given by the standard deviation of the uniform distribution, i.e. $\sigma(L) = L/\sqrt{12}$, where L is the length in the relevant dimension.

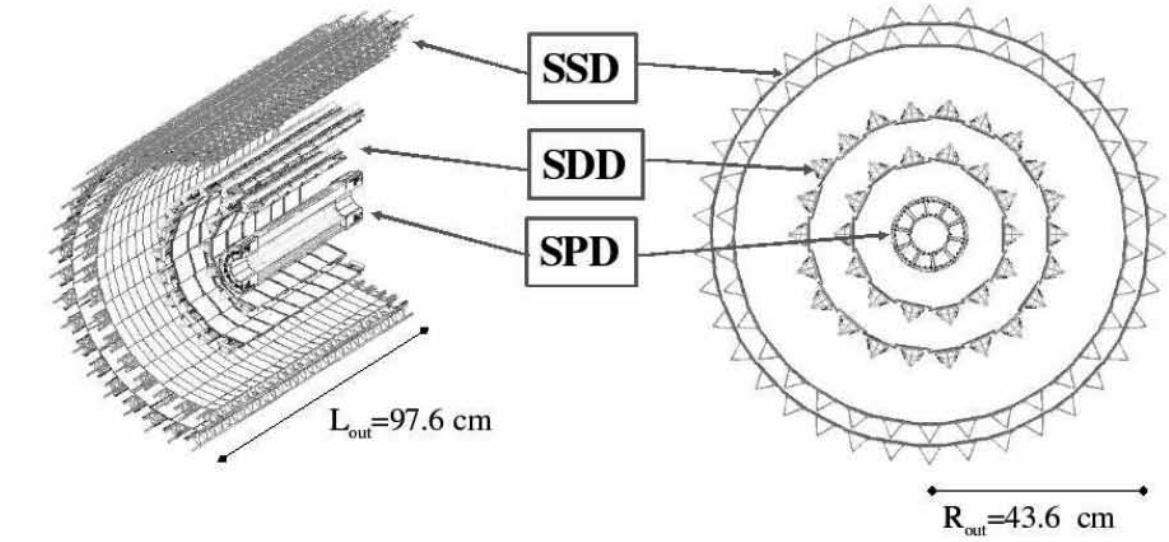

Figure 3.1: Layout of the ITS.

FIGURE 3.3: Layout of the ITS sub-detector, comprising of silicon pixel (SPD), drift (SDD) and strip (SSD) detectors [19].

Table 3.1: Dimensions of the ITS detectors (active areas).

Layer	Type	r (cm)	$\pm z$ (cm)	Area (m^2)	Channels
1	pixel	3.9	14.1	0.07	3 276 800
2	pixel	7.6	14.1	0.14	6 553 600
3	drift	15.0	22.2	0.42	43 008
4	drift	23.9	29.7	0.89	90 112
5	strip	38.0	43.1	2.20	1 148 928
6	strip	43.0	48.9	2.80	1 459 200
	Total area			6.28	

- dE/dx **measurements:** In order to assist in particle identification, analogue readouts are needed on a number of planes, reporting a precise energy loss measurements. The range of these analogue readouts must be sufficient to provide energy loss readings for low momentum particles. For the drift detectors, the readout has a charge range of (0.04-32) fC.
- **Material Budget:** Low-p_T particles undergo multiple scattering as they travel through detectors. In order to minimise the effect of these deflections on measurements, the amount of material through which particles travel must be minimised. The integral of the material traversed by a particle in the ITS travelling radially outward against radius is shown in Figure 3.4.
- **Granularity:** Track densities of up to $dN/d\eta \approx 8000$ means that the ITS must be able to detect in the region of 15 000 tracks simultaneously. In order to ensure individual tracks are identified, the occupancy (or percentage of cells through which tracks travel at any given time) must remain small, resulting in each layer of the ITS requiring several million cells.
- **Spatial Precision:** In order to detect charmed particles, the impact parameter resolution must be better than 100 μm in the $r\phi$ plane. The impact parameter resolution is largely determined by the spatial precision of the detectors. The spatial precision of the various layers is given in Table 3.1.

momentum, highly ionising particles, down to the lowest momentum at which tracks can still be reconstructed. This feature gives the ITS stand-alone capability as a low-p_t particle spectrometer. The main parameters for each of the three detector types are summarized in table 3.2. The overall cooling system of the ITS outer layers has been designed [28–30] to satisfy the stringent requirements of the TPC in terms of temperature stability and uniformity.

The momentum and impact parameter resolution for low-momentum particles are dominated by multiple scattering effects in the material of the detector; therefore the amount of material in the active volume has been kept to a minimum. The silicon detectors used to measure ionisation densities (drift and strips) must have a minimum thickness of approximately 300 μm to provide acceptable signal-to-noise ratio. In addition, detectors must overlap to cover the solid angle entirely. Therefore, the detectors effective thickness amounts to 0.4% of X_0. The additional material in the active volume, i.e. electronics, cabling, support structure, and cooling system, has been kept at a comparable effective thickness (table 3.3). The values in the table are for the detector as built, and they are remarkably close to the goals set at the time of the design [11]. Figure 3.2 shows the integral of the material traversed by a particle crossing perpendicularly the ITS as a function

- **Radiation Levels:** The total dose received during 10 years of operation is expected to exceed 130 krad for the inner pixel layer and 2 krad for the outer strip layer. The materials chosen for each layer were tested for their ability to withstand these radiation doses.

- **Readout Time:** The pixel layers of the ITS are read out when triggered by the muon arm trigger, in order to determine the position of the primary vertex, and are required to have a readout time of below 400 μs.

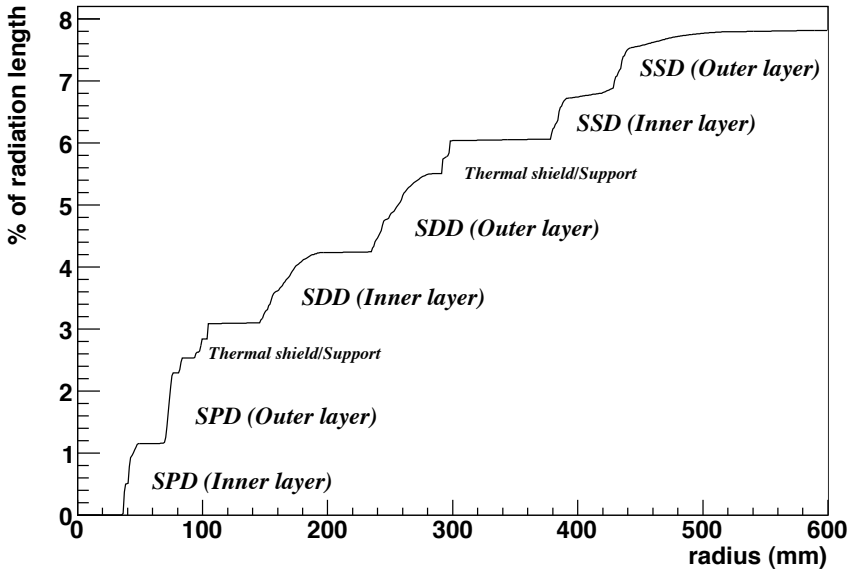

FIGURE 3.4: Integral of material thickness traversed by a particle traveling radially outward from the primary vertex, through the ITS detectors and support structures, shown as a function of radius [19]. The radiation length X_0 is defined as the mean distance over which an energetic electron loses all but 1/e of its energy via electronic bremsstrahlung.

TABLE 3.1: Parameters of the ITS pixel, drift and strip detectors [23].

Parameter	Unit	Silicon Pixel	Silicon Drift	Silicon Strip
Radius (inner layer)	cm	3.9	15.0	38.0
Radius (outer layer)	cm	7.6	23.9	43.0
Spatial precision ($r\phi$)	μm	12	35	20
Spatial precision (z)	μm	100	25	830
Cell size ($r\phi \times z$)	μm^2	50 $\times$ 425	202 $\times$ 294	85 $\times$ 40000
Total number of cells (millions)		9.84	23	2.6

The inner two layers of the ITS are silicon pixel detectors (SPDs), in order to cope with the high track densities at smaller radii: pixel detectors consist of a large number of small cells, known as pixels, which can be triggered individually by ionising particles. The two pixel layers are vital for the determination of the primary vertex. The readout is binary, with a cell's digital signal changing when the deposited energy is above a 2 keV threshold. Each cell contains a p-n junction with a reverse biased current, creating a depletion zone in which no mobile charge carriers are present. Particles travelling through this depletion zone generate charge carriers (at an average of roughly one electron-hole pair per 3.6 eV of deposited energy) which, under the electric field across the p-n junction, create a current that is interpreted as a signal [24] or a "hit". The signal is ignored if below the minimum threshold (equivalent to the signal emerging from a 2 keV electron in the ITS). Each cell measures 50 μm ($r\phi$) $\times$ 425 μm (z) and cells are arranged in 256 $\times$ 160 cell modules. Each module is connected to an electronics chip and support mounting. As there is a small dead-zone on the edge of each module, it is necessary to overlap them azimuthally, as shown in Figure 3.5.

3.3 δ Rays and the Effect of Multiple Scattering in SPDs

It is not only within the detector that ionising particles deposit energy via microscopic collisions, but also while travelling through the various support structures and electronics of individual detectors, as well as the accelerator beam pipe. While individual collisions occur randomly and are difficult to describe, one can create a macroscopic approximation that is suitable for use in a Monte-Carlo simulation. The commonly used macroscopic models are described in the next chapter.

Ionising particles travelling through SPDs are deflected by collisions, affecting the resolution of track hit positions in SPDs. In the presence of a magnetic field, a charged particle will travel in a helix, with a radius of curvature given by

$$R = \frac{p_T}{0.3B}, \tag{3.1}$$

with the magnetic field B in Teslas, p_T in units of GeV/c and R in metres. As the particle will lose energy through each layer of SPDs, the radius of curvature

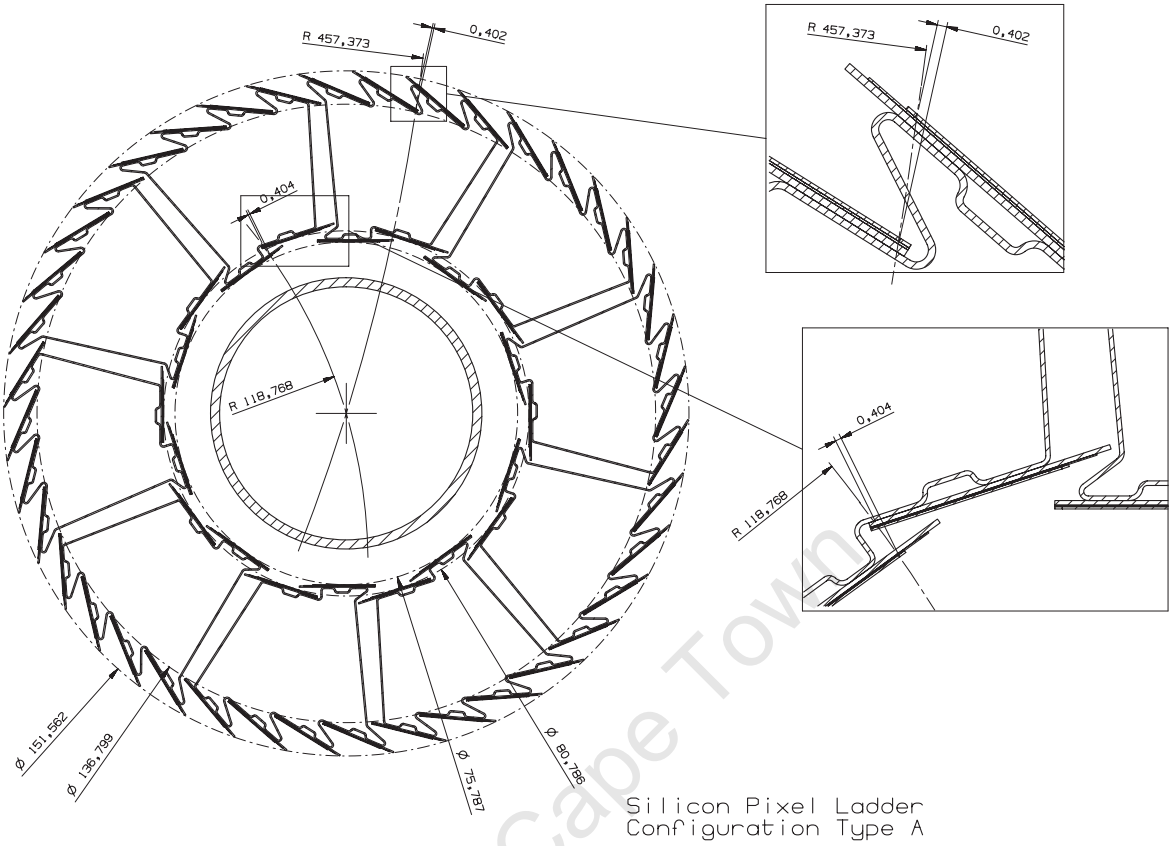

FIGURE 3.5: The azimuthal arrangement of pixel modules in a cylinder around the beam pipe ensures that the entire angular range is covered. As tracks emerge in helices due to the applied magnetic field, tracks with certain curvature radii may still pass undetected. These are shown in the inserts on the right. The maximum curvature radii for which tracks may pass undetected through the inner and outer layers are 119 mm and 457 mm respectively [23]. The inner and outer radii of the layers are also shown.

of the particle will take on a number of values during its path. As the energy loss can be estimated, one can correct for the change in R when calculating the impact parameter.

In rare cases, ionising radiation can provide sufficient energy to dislodge an electron from an atom with sufficient kinetic energy to act as ionising radiation itself. These "knock-on" electrons are known as δ rays and, given sufficient kinetic energy, can create additional hits on SPDs. As the ITS SPDs are pivotal to impact parameter resolution, this study will focus on the effect of δ rays, specifically on SPD hits and the reconstructed impact parameters.

3.4 Possible Upgrades to the ITS SPDs

To improve the impact parameter resolution, three possible modifications to the ITS SPDs can be considered:

- **Decrease the material budget:** Decreasing the average number of radiation lengths traversed by particles through the SPDs would decrease the number of δ rays produced. The effect of scattering and energy loss on impact parameter resolution would also be minimised.
- **Decrease pixel size:** By decreasing the size of individual pixels in the SPDs, the spatial resolution of hits, and hence the impact parameter resolution would be improved. The danger of this approach is that δ rays produced in the detector would be more likely to traverse multiple pixels, as the distance travelled within each pixel is decreased. This would lead to erroneous hit generation and negate some of the improvements to the impact parameter resolution if the behaviour of δ rays produced is not well understood.
- **Modify detector layout:** Bringing the layers radially inward as much as possible would improve the impact parameter resolution by improving the accuracy of hit position measurements: If the inner layer is positioned against the beam pipe, then any deflection resulting from interaction with the beam pipe will barely affect the position of hits in the inner layer.

In this study, a combination of the three modifications was chosen. Simulations were also run with an artificially thin beam pipe, to discern which of the factors had the most noticeable effect on impact parameter resolution. The modified geometry investigated is compared with the original geometry in Chapter 5.

Chapter 4

Monte-Carlo Simulations in High Energy Physics

4.1 Monte-Carlo Simulations of Collisions

To simulate the passage of energised particles through matter, one can use a Monte-Carlo based particle transport package. These packages track particles through a user-defined geometry and, at each step, evaluate the probability of selected physical processes occurring, based on experimentally verified data. At each step, discrete events, such as decays, interactions with other particles or pair production may therefore occur, while continuous processes, such as multiple scattering (due to the medium) and energy loss, occur at each step in the track's simulation. The manner in which all physical processes occur depends on the medium through which the particle travels, as well as its particle type and kinetic energy. Physical processes can create new particles to track, known as secondary or daughter particles. Primary particles are generated either by the user's specification, or by a Monte-Carlo event generator, such as Pythia [25], which can simulate the generation of particles emerging from a real-world situation (such as proton-proton collisions or heavy ion collisions).

The data analysis framework ROOT [26], used in this study, contains an interface to a virtual transport package [27], to which various actual transport packages, such as GEANT3 [28], can be connected. The advantage of using this interface is that the geometry of the simulation, the generation of primary particles and any

additional user instructions can be written once and run using multiple transport packages with minimal reconfiguration. This allows one to easily compare simulations using different transport packages, starting from the same initial conditions.

4.2 Particle Transport using GEANT3

The transport of particles in a GEANT3 event is performed using a First-In-Last-Out (FILO) stack, onto which primary particles (either specified by the user or randomly generated) are pushed. Generated secondary particles are also pushed onto the stack. The outline of the processes performed at each step of a particle's propagation through a medium is as follows:

- **Fetch particle from stack**: (Only once per particle) The particle's details are fetched from the top of the particle stack. The number of interaction lengths[1] before each discrete process occurs is sampled from a random number generator.
- **Evaluate distance to the next interaction point**: The distance until each discrete process occurs is calculated as the product of the interaction length and the remaining number of interaction lengths. The step distance is taken as the minimum of these distances. The step distance is constrained by user specified limits, energy or time-of-flight cuts and limits for which utilized approximations of continuous physical processes are valid. In addition, step distance is decreased in the region of medium boundaries to ensure accurate propagation up to the interface.
- **Transport particle**: The particle is transported on a straight line or in a helix (depending on the charge) in the presence of a magnetic field.
- **Simulation of continuous processes**: Simulation of continuous processes, such as energy loss and multiple scattering, is performed.
- **Simulation of selected discrete processes**: Discrete processes, for which the number of remaining interaction lengths has reached zero, are simulated. These may include particle decay, pair production, δ ray production or a

[1]The interaction length is defined as the inverse of the cross section of a discrete process occurring in the current medium.

number of other user-selectable processes. The number of interaction lengths until the next occurrence of the same process is again sampled and the number of remaining interaction lengths for each process is updated.

Discussions of the theoretical descriptions of the most important physical processes in this experiment, as well as their simulation in GEANT3, follow below.

4.2.1 Continuous Energy Loss

Relativistic particles travelling through a medium lose energy, primarily via ionisation or excitation of individual atoms [29]. While on a microscopic level this is a discrete process, involving the interaction of the particle with an enormous number of individual atoms, it can easily be approximated at a macroscopic level as a continuous process if the medium is uniform. The rate of energy loss can then be calculated, based on the properties of the medium and of the particle itself. One such approximation is the Bethe-Bloch equation, which for a particle of charge z, travelling through a medium with atomic number Z and mass number A is [30]:

$$-\left\langle \frac{dE}{dx} \right\rangle = Kz^2 \frac{Z}{A}\frac{1}{\beta^2}\left[\frac{1}{2}\ln\frac{2m_e c^2\beta^2\gamma^2 T_{\max}}{I^2} - \beta^2\right], \tag{4.1}$$

where $K = 4\pi N_A r_e^2 m_e c^2$, I is the mean excitation energy of struck atoms and $T_{\max}$ is the maximum kinetic energy that can be imparted to a free electron in a single collision, which, for a particle of mass M, is:

$$T_{\max} = \frac{2m_e c^2\beta^2\gamma^2}{1 + 2\gamma m_e/M + (m_e/M)^2}. \tag{4.2}$$

At very high energies, an additional term of the order of $\ln\beta\gamma$ is added to Equation 4.1 due to the effects of medium polarisation [29].

In GEANT3, tables of $\left\langle \frac{dE}{dx} \right\rangle$ for a range of energies through each medium included in the simulation are calculated prior to particle transport. During particle transport, the approximate value of $\left\langle \frac{dE}{dx} \right\rangle$ is then calculated for a given particle energy by linearly interpolating between values in the tables. The energy lost in a step is sampled from a bounded Landau distribution[2] with mean $\left\langle \frac{dE}{dx} \right\rangle$ [28].

[2]As the average value of the standard Landau distribution is infinite, one can bound the Landau distribution such that any values above a maximum are rejected, ensuring that the average fluctuation from $\left\langle \frac{dE}{dx} \right\rangle$ is zero.

4.2.2 Multiple Scattering

Charged particles travelling through a medium are deflected by Coulomb interactions with nuclei, resulting in a large number of small-angle scatters. This scattering follows a Gaussian distribution approximately, with a width of

$$\theta_0 = \frac{13.6 \text{ MeV}}{\beta cp} z\sqrt{x/X_0}\,[1 + 0.038 \ln(x/X_0)]\,, \tag{4.3}$$

where p and z are the momentum and charge of the incident particle respectively, x is the distance traversed in the medium and X_0 is the medium's radiation length, defined as the mean distance over which an energetic electron loses all but 1/e of its energy via electronic bremsstrahlung [30].

While this approximation is sufficiently accurate for a large range of values of x/X_0, its application in Monte-Carlo techniques is limited as the r.m.s angle θ_0 changes when the distance x is traversed in two steps x_1 and x_2:

$$\theta_0(x) = \theta_0(x_1 + x_2) \neq \sqrt{\theta_0^2(x_1) + \theta_0^2(x_2)}.$$

In GEANT3, this problem is alleviated by either using an approximation of the order of $\sqrt{x}$, or by a more complete simulation of Molière scattering [28]. Molière's theory of multiple scattering requires the following conditions:

- The scattering from a single step must result in a *small* deflection. This limits the maximum step distance for which Molière scattering can be simulated accurately.
- The *number* of scatters expected in a step, Ω_0, is large. Below a certain threshold (taken as $\Omega_0 < 20$ in GEANT3), individual elastic scatterings are simulated.
- The theory is only applicable in a semi-infinite homogeneous medium, thus requiring careful application close to media boundaries.
- Energy loss due to individual scattering must be negligible. This can be achieved by keeping the step size small.

A complete description of Bethe's derivation of Molière scattering can be found in [31]. The angular distribution is given by:

$$f(\theta)\theta d\theta = \sqrt{\frac{\sin\theta}{\theta}} f_r(\eta)\eta d\eta, \tag{4.4}$$

where $f_r(\eta)$ is Bethe's expansion, given in [31], and η is the reduced angle, defined as

$$\eta = \frac{\theta}{\chi_c\sqrt{B}}, \tag{4.5}$$

with $B - \ln B = \ln \Omega_0$ and the critical scattering angle χ_c being a property of the medium and of the incident particle energy, described in [28].

4.2.3 δ Ray Production

Energetic secondary electrons with kinetic energy, T, well above the ionisation energy, I, are produced by high energy charged particles traveling through a medium, with a distribution given by:

$$\frac{d^2N}{dTdx} = \frac{1}{2}Kz^2\frac{Z}{A}\frac{1}{\beta^2}\frac{F(T)}{T^2}, \tag{4.6}$$

where $F(T)$ is defined as:

$$F(T) = \begin{cases} 1 - \beta^2\frac{T}{T_{\max}} & : \text{Spin-0 incident particles} \\ 1 - \beta^2\frac{T}{T_{\max}} + \frac{T^2}{2E^2} & : \text{Spin-}\frac{1}{2}\text{ incident particles} \end{cases}$$

and $T_{\max}$, K, z, Z and A are defined in Section 4.2.1. Figure 4.1 shows the average number of δ rays produced by a 1 GeV pion travelling through 500 μm of beryllium, for which $T_{\max} \approx 48$ MeV. One can see that high energy δ rays are rarely produced.

If one considers continuous energy loss via ionisation and atomic excitations, as discussed in Section 4.2.1, restricted to the region $T \leq T_{\text{cut}} \leq T_{\max}$, the average energy loss rate is then

$$-\left\langle\frac{dE}{dx}\right\rangle_{T<T_{\text{cut}}} = Kz^2\frac{Z}{A}\frac{1}{\beta^2}\left[\frac{1}{2}\ln\frac{2m_ec^2\beta^2\gamma^2T_{\text{cut}}}{I^2} - \frac{\beta^2}{2}\left(1 + \frac{T_{\text{cut}}}{T_{\max}}\right)\right]. \tag{4.7}$$

$$T_{\max} = \frac{2\gamma m_e}{1 + 2\gamma m_e/M + (m_e/M)^2} \quad (2)$$

where M is the mass of the incident particle. If one considers a pion of kinetic energy 1GeV traveling through a medium of Beryllium, the cuttoff energy $T_{\max} \approx 48$MeV. The distribution of δ-rays in this case is shown in Figure 2.

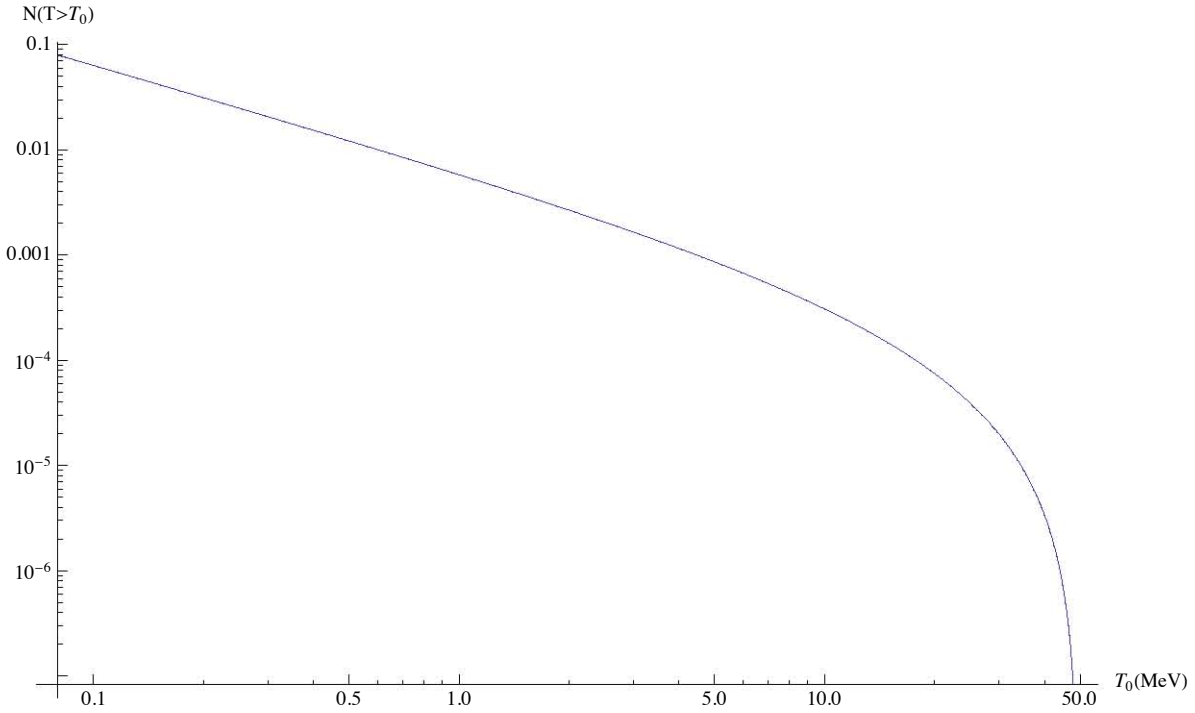

Figure 2: Average Number of δ-rays produced per track by a 1GeV pion in 500μm of Beryllium with k energy $T > T_0$.

FIGURE 4.1: Average number of δ rays produced by a 1 GeV incident pion in 500 μm of beryllium with kinetic energy $T > T_0$. As the average energy of δ rays produced is well below the incident pion energy, the rate of energy loss remains approximately constant.

Most of the electrons produced are in the keV range. This report focuses on energies between 100keV and 1MeV, as below 100keV, average electron ranges are too short to propagate far enough to reach neighbouring pixel detectors, while above 1MeV, too few electrons are produced to warrant an analysis.

The standard Bethe-Bloch equation (Equation 4.1) is recovered as $T_{\text{cut}} \to T_{\max}$. Furthermore, it can be shown that the weighted integral of Equation 4.6 is equal to the difference between Equations 4.1 and 4.7:

Table 1: Properties of δ-rays produced by 1GeV Pion in 500μm of Beryllium

$$\int_{T_{\text{cut}}}^{T_{\max}} T \frac{d^2N}{dTdx} dT = \left\langle \frac{dE}{dx} \right\rangle - \left\langle \frac{dE}{dx} \right\rangle_{T<T_{\text{cut}}}. \quad (4.8)$$

δ-ray kinetic energy (T_0)	δ-rays per track with $T > T_0$	Emission angle	Range: Be (r_0)	Range: Al (r_0)
0.1 MeV	6.3×10^{-2}	70°	93μm (1.7×10^{-2} g.cm^{-2})	69μm (1.3×10^{-2} g.cm
1.0 MeV	5.8×10^{-3}	45°	2.9mm (0.54g.cm^{-2})	2.0mm (0.37g.cm^{-2}

The consequence of this is that when simulating energy loss via Monte-Carlo methods, one can arbitrarily choose a value of T_{cut} above which δ-ray production is simulated explicitly as a discrete process and below which energy loss is simulated as a continuous process. Equation 4.8 guarantees that the total energy loss rate will, at least on average, be unaffected by the choice of T_{cut}. GEANT3 takes this approach and allows the user to specify the cut-off energies for δ-ray production in each medium. Energy and momentum conservation dictate that a δ-ray with kinetic energy T_ξ and momentum p_e will be produced at a polar angle θ with the

To validate the behaviour of these δ-rays in the ALICE simulation framework, the passage of these low energy electrons through the relevant materials should be compared to accepted results. The paper "Transmission and Reflection of Electrons by Foils" [2] by Seltzer and Berger gives a number of results from a Monte-Carlo simulation using the ETRAN code that have been validated against experimental measurements, and thus provides accepted results to which one can compare the particle transport code of the ALICE simulation framework, the GEANT3 Monte-Carlo transport package. GEANT3 is widely used and while more modern and frequently maintained codes, such as GEANT4 and FLUKA exist, GEANT3 is used across the ALICE experiment.

Simulation Setup

incident particle such that [30]

$$\cos\theta = (T_e/p_e)(p_{\max}/T_{\max}), \tag{4.9}$$

where $p_{\max}$ is the momentum of an electron with maximum possible energy $T_{\max}$, given by Equation 4.2.

4.3 Validation of δ Ray Behaviour in GEANT3

In order to validate the treatment of δ rays in the GEANT3 transport package, a simulation of the passage of low energy electrons through thin foils was performed, and the results of the simulation were compared against established Monte-Carlo results, as well as experimental measurements. The paper "Transmission of electrons by thin foils" [32] describes the validation of the Monte-Carlo code "ETRAN", used for charged particle transport. The paper describes the simulation of the passage of electrons through thin foils of various material, and compares the results of this simulation with experimental data. For this simulation, single electrons were propagated along the y-axis in a vacuum towards a thin foil of variable thickness. The passage through the foil was tracked and the positions and energies of the primary and secondary (i.e δ ray) electrons as they eventually left the simulation's defined bounding box were recorded. Electrons leaving the bounding box with $y > 0$ were considered to have been transmitted through the foil, while those with $y < 0$ were considered reflected by the foil. A diagram of the simulation setup is shown in Figure 4.2.

Simulations were run with both beryllium and aluminium foils, as these materials are present in the ALICE ITS [17]. The simulation was run for incident electron energies ranging from 100 keV - 400 keV with various foil thicknesses[3], to match the parameters simulated in [32]. For each combination of parameters, 100 000 events were simulated. For comparisons at higher energies, 20 000 events per simulation configuration were simulated at energies up to 8 MeV. The calculated quantities were:

- **Angular Distribution** of transmitted electrons, with respect to the y-axis.

[3]Thickness is shown in both mils and mg/cm^2. 1 mil = 25.4 μm. Conversion from mils to mg/cm^2 is dependent on material density.

- **Energy Distribution** of transmitted electrons, including mean energy E_{av}, most probable energy E_p, and the distribution's full-width-half-maximum (FWHM).

- **Transmission Number Coefficient (T_N)**, defined as the ratio of the total number of outgoing electrons in the $y > 0$ hemisphere to the number of incoming electrons. This number can rise above unity if the number of secondary electrons ionised by incident electrons more than compensates for the number of absorbed and reflected electrons.

- **Reflection Number Coefficient (R_N)**, similarly defined as the ratio of the total number of outgoing electrons in the $y < 0$ hemisphere to the number of incoming electrons.

- **Transmission and Reflection Energy Coefficients (T_E and R_E)**, defined as the fraction of total incident energy carried by outgoing transmitted and reflected electrons respectively.

Tables 4.1 and 4.3 show the cumulative angular distributions of transmitted electrons through beryllium and aluminium respectively. Tables 4.2 and 4.4 show the entries obtained in [32] corresponding to Tables 4.1 and 4.3 respectively. These

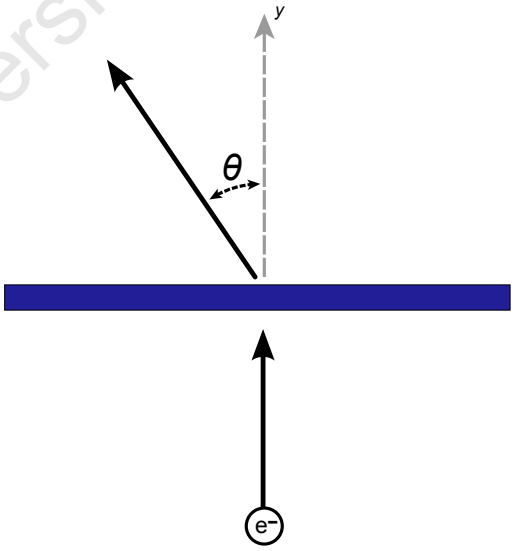

FIGURE 4.2: Simulation setup for δ ray validation. The deflection angle θ is defined as the angle between the y axis and the vector drawn from the centre of the foil to the final position of the outgoing electron.

tables show that, above incident energies of 300 keV, there are no significant deviations (below 5% relative difference) in the angular distribution of transmitted electrons calculated from the GEANT3 simulation to those calculated from the simulation in [32].

TABLE 4.1: Cumulative angular distribution of transmitted electrons in beryllium. The quoted quantities are the fraction of transmitted electrons with an outgoing angle (with respect to the incident beam axis) of between 0 °and θ.

Foil thickness		Cone angle, θ						
(mils)	(mg/cm^2)	5 °	10 °	15 °	20 °	30 °	45 °	60 °
Beryllium								
				E_0=100 keV				
2	9.40	0.008	0.031	0.073	0.124	0.263	0.491	0.713
3	14.10	0.004	0.020	0.052	0.095	0.201	0.394	0.621
				E_0=150 keV				
2	9.40	0.019	0.075	0.157	0.260	0.480	0.746	0.897
3	14.10	0.011	0.048	0.102	0.175	0.352	0.618	0.819
5	23.50	0.009	0.037	0.075	0.125	0.257	0.491	0.709
				E_0=200 keV				
2	9.40	0.035	0.132	0.267	0.413	0.670	0.881	0.960
3	14.10	0.023	0.082	0.173	0.281	0.507	0.772	0.914
5	23.50	0.013	0.049	0.106	0.178	0.361	0.629	0.832
				E_0=300 keV				
2	9.40	0.075	0.259	0.478	0.664	0.870	0.963	0.987
3	14.10	0.047	0.171	0.340	0.507	0.758	0.923	0.976
5	23.50	0.026	0.093	0.196	0.320	0.566	0.818	0.937
				E_0=400 keV				
2	9.40	0.127	0.397	0.647	0.807	0.935	0.980	0.992
3	14.10	0.079	0.273	0.491	0.670	0.874	0.964	0.987
5	23.50	0.041	0.152	0.308	0.472	0.733	0.916	0.973

TABLE 4.2: Cumulative angular distribution of transmitted electrons in beryllium, obtained in [32].

Foil thickness		Cone angle, θ						
(mils)	(mg/cm^2)	5 °	10 °	15 °	20 °	30 °	45 °	60 °
Beryllium								
				E_0=100 keV				
2	9.40	0.012	0.050	0.111	0.189	0.378	0.659	0.863
3	14.10	0.013	0.051	0.111	0.182	0.368	0.650	0.858
				E_0=150 keV				
2	9.40	0.024	0.086	0.185	0.301	0.539	0.802	0.934
3	14.10	0.015	0.061	0.129	0.218	0.421	0.702	0.888
5	23.50	0.013	0.050	0.107	0.176	0.360	0.645	0.853
				E_0=200 keV				
2	9.40	0.034	0.130	0.269	0.420	0.693	0.912	0.977
3	14.10	0.025	0.093	0.196	0.317	0.558	0.820	0.942
5	23.50	0.014	0.056	0.122	0,208	0.404	0.691	0.880
				E_0=300 keV				
2	9.40	0.074	0.261	0.486	0.678	0.896	0.978	0.993
3	14.10	0.050	0.185	0.365	0.546	0.806	0.949	0.986
5	23.50	0.027	0.104	0.218	0.354	0.617	0.860	0.957
				E_0=400 keV				
2	9.40	0.135	0.411	0.663	0.826	0.947	0.985	0.994
3	14.10	0.071	0.255	0.481	0.675	0.897	0.979	0.994
5	23.50	0.040	0.152	0.317	0.486	0.756	0.937	0.985

TABLE 4.3: Cumulative angular distribution of transmitted electrons in aluminium. The quoted quantities are the fraction of transmitted electrons with an outgoing angle (with respect to the incident beam axis) of between 0°and θ.

Foil thickness		Cone angle, θ						
(mils)	(mg/cm^2)	5 °	10 °	15 °	20 °	30 °	45 °	60 °
Aluminium								
				E_0=100 keV				
$\frac{1}{2}$	3.43	0.013	0.048	0.103	0.172	0.341	0.599	0.805
1	6.86	0.006	0.029	0.059	0.104	0.215	0.423	0.651
2	13.72	0.006	0.020	0.036	0.063	0.148	0.323	0.535
				E_0=150 keV				
$\frac{1}{2}$	3.43	0.026	0.096	0.201	0.321	0.565	0.810	0.928
1	6.86	0.011	0.044	0.093	0.162	0.328	0.585	0.794
2	13.72	0.007	0.029	0.063	0.107	0.223	0.448	0.672
				E_0=200 keV				
$\frac{1}{2}$	3.43	0.046	0.160	0.321	0.483	0.735	0.909	0.969
1	6.86	0.020	0.074	0.155	0.260	0.478	0.745	0.894
2	13.72	0.010	0.037	0.081	0.144	0.292	0.542	0.754
				E_0=300 keV				
$\frac{1}{2}$	3.43	0.091	0.308	0.537	0.715	0.893	0.969	0.988
1	6.86	0.040	0.146	0.296	0.449	0.710	0.900	0.967
2	13.72	0.017	0.069	0.144	0.245	0.457	0.728	0.885
				E_0=400 keV				
$\frac{1}{2}$	3.43	0.146	0.449	0.692	0.833	0.943	0.981	0.991
1	6.86	0.065	0.231	0.435	0.615	0.838	0.954	0.984
2	13.72	0.029	0.110	0.229	0.368	0.619	0.854	0.947

TABLE 4.4: Cumulative angular distribution of transmitted electrons in aluminium, obtained in [32].

Foil thickness		Cone angle, θ						
(mils)	(mg/cm^2)	5 °	10 °	15 °	20 °	30 °	45 °	60 °
Aluminium								
				E_0=100 keV				
$\frac{1}{2}$	3.43	0.013	0.052	0.112	0.191	0.381	0.654	0.855
1	6.86	0.010	0.038	0.087	0.152	0.317	0.591	0.816
2	13.72	0.011	0.041	0.084	0.150	0.314	0.605	0.815
				E_0=150 keV				
$\frac{1}{2}$	3.43	0.022	0.088	0.186	0.305	0.560	0.826	0.943
1	6.86	0.013	0.052	0.112	0.190	0.374	0.645	0.849
2	13.72	0.011	0.041	0.084	0.150	0.314	0.605	0.815
				E_0=200 keV				
$\frac{1}{2}$	3.43	0.034	0.127	0.262	0.415	0.694	0.915	0.977
1	6.86	0.018	0.071	0.152	0.255	0.480	0.757	0.909
2	13.72	0.011	0.044	0.097	0.165	0.339	0.615	0.834
				E_0=300 keV				
$\frac{1}{2}$	3.43	0.091	0.305	0.528	0.707	0.894	0.970	0.989
1	6.86	0.041	0.150	0.302	0.462	0.719	0.910	0.973
2	13.72	0.020	0.077	0.164	0.267	0.487	0.749	0.907
				E_0=400 keV				
$\frac{1}{2}$	3.43	0.080	0.296	0.548	0.756	0.954	0.997	0.999
1	6.86	0.050	0.197	0.381	0.569	0.826	0.958	0.988
2	13.72	0.025	0.097	0.209	0.343	0.611	0.859	0.953

Table 4.5 shows the relationship between the incident electron energy E_0 and transmitted electrons' mean energy E_{av}, most probable energy E_p and the distribution's full-width-half-maximum (FWHM) W, with corresponding entries from [32] shown in Table 4.6. While there is good agreement with the results of [32] for the ratios of E_{av} and E_p to E_0, the deviation from the results of [32] in the ratios of the distribution width parameter, W, to E_p and E_0 shows that, at incident electron energies of up to 400 keV, the distribution of transmitted electrons from the GEANT3 simulation differs from the results of the simulation performed in [32]. However, there is no experimental evidence given in [32] to confirm which is the more accurate simulation. Thus, the disagreement does not affect the validity of the use of GEANT3 for δ ray investigations.

TABLE 4.5: Energy distribution parameters, showing the relationship between incident energy E_0 and the mean energy E_{av}, most probable energy E_p and full-width-half-maximum W of transmitted electrons in beryllium and aluminium.

Foil thickness (mils)	Foil thickness (mg/cm^2)	Quantity calculated	Incident energy (keV) 100	150	200	300	400
Beryllium							
2	9.40	E_{av}/E_0	0.539	0.787	0.872	0.931	0.952
3	14.10	E_{av}/E_0	0.283	0.644	0.796	0.893	0.927
5	23.50	E_{av}/E_0	0.000	0.351	0.619	0.814	0.878
2	9.40	E_p/E_0	0.623	0.817	0.892	0.953	0.962
3	14.10	E_p/E_0	0.323	0.702	0.849	0.924	0.951
5	23.50	E_p/E_0	0.021	0.416	0.699	0.853	0.908
2	9.40	W/E_0	0.132	0.054	0.038	0.021	0.016
3	14.10	W/E_0	0.201	0.090	0.057	0.028	0.017
5	23.50	W/E_0	-	0.219	0.116	0.043	0.029
2	9.40	W/E_p	0.212	0.066	0.043	0.023	0.016
3	14.10	W/E_p	0.623	0.128	0.067	0.030	0.018
5	23.50	W/E_p	-	0.526	0.166	0.050	0.032
Aluminium							
$\frac{1}{2}$	3.43	E_{av}/E_0	0.854	0.928	0.956	0.974	0.981
1	6.86	E_{av}/E_0	0.677	0.842	0.904	0.949	0.963
2	13.72	E_{av}/E_0	0.396	0.638	0.782	0.888	0.927
$\frac{1}{2}$	3.43	E_p/E_0	0.892	0.943	0.968	0.979	0.984
1	6.86	E_p/E_0	0.761	0.885	0.924	0.964	0.973
2	13.72	E_p/E_0	0.500	0.739	0.837	0.921	0.952
$\frac{1}{2}$	3.43	W/E_0	0.073	0.042	0.027	0.020	0.017
1	6.86	W/E_0	0.171	0.061	0.036	0.023	0.015
2	13.72	W/E_0	0.272	0.132	0.071	0.033	0.023
$\frac{1}{2}$	3.43	W/E_p	0.082	0.045	0.027	0.021	0.017
1	6.86	W/E_p	0.225	0.069	0.039	0.024	0.016
2	13.72	W/E_p	0.543	0.179	0.085	0.035	0.024

TABLE 4.6: Energy distribution parameters obtained in [32].

Foil thickness (mils)	Foil thickness (mg/cm^2)	Quantity calculated	Incident energy (keV) 100	150	200	300	400
Beryllium							
2	9.40	E_{av}/E_0	0.557	0.799	0.883	0.933	0.954
3	14.10	E_{av}/E_0	0.332	0.672	0.813	0.900	0.930
5	23.50	E_{av}/E_0	-	0.418	0.650	0.825	0.885
2	9.40	E_p/E_0	0.642	0.841	0.908	0.952	0.969
3	14.10	E_p/E_0	0.362	0.745	0.850	0.925	0.950
5	23.50	E_p/E_0	-	0.479	0.713	0.865	0.911
2	9.40	W/E_0	0.186	0.078	0.040	0.021	0.014
3	14.10	W/E_0	0.284	0.123	0.073	0.033	0.020
5	23.50	W/E_0	-	0.259	0.147	0.062	0.036
2	9.40	W/E_p	0.290	0.093	0.045	0.022	0.014
3	14.10	W/E_p	0.783	0.166	0.086	0.086	0.021
5	23.50	W/E_p	-	0.541	0.206	0.071	0.040
Aluminium							
$\frac{1}{2}$	3.43	E_{av}/E_0	0.842	0.930	0.963	0.976	0.984
1	6.86	E_{av}/E_0	0.653	0.835	0.909	0.952	0.965
2	13.72	E_{av}/E_0	0.115	0.638	0.781	0.892	0.929
$\frac{1}{2}$	3.43	E_p/E_0	0.901	0.954	0.971	0.985	0.990
1	6.86	E_p/E_0	0.754	0.894	0.936	0.967	0.978
2	13.72	E_p/E_0	0.392	0.742	0.849	0.925	0.953
$\frac{1}{2}$	3.43	W/E_0	0.091	0.038	0.026	0.015	0.010
1	6.86	W/E_0	0.185	0.076	0.048	0.025	0.016
2	13.72	W/E_0	0.326	0.197	0.102	0.046	0.026
$\frac{1}{2}$	3.43	W/E_p	0.101	0.040	0.027	0.015	0.010
1	6.86	W/E_p	0.245	0.085	0.051	0.025	0.016
2	13.72	W/E_p	0.832	0.266	0.120	0.049	0.028

Table 4.7 shows the various coefficients (T_N, R_N, T_E and R_E) calculated from the GEANT3 simulation. Statistical errors in number coefficients were estimated using the binomial distribution's standard deviation:

$$\left(\frac{\sigma(T_N)}{T_N}\right)^2 = h^{-1}\left(\frac{1-T_N}{T_N}\right), \tag{4.10}$$

where h is the size of the sample set, while errors in the energy coefficients were derived from errors in the number coefficients and average energy:

$$\left(\frac{\sigma(T_E)}{T_E}\right)^2 = \left(\frac{\sigma(T_N)}{T_N}\right)^2 + \left(\frac{\sigma(E_{\text{av}})}{E_{\text{av}}}\right)^2. \tag{4.11}$$

Table 4.8 shows the corresponding entries obtained in [32]. Plots of these quantities, which were made against the energy-independent ratio z/r_0 (where z is the foil thickness and r_0 is the mean range of electrons with a given energy in the simulated medium), can be seen in Figures 4.3, 4.4 and 4.5. These plots were reproduced from [32], with the legends referring to work discussed therein. Figure 4.4 shows that deviation from experimental data occurs at 100 keV incident electron energy, but not at 500 keV. Figure 4.5 shows that the behaviour of low energy electrons in GEANT3 at the interface between media disagrees significantly with experimental results, while Table 4.7 shows that significant deviation from the results in [32] (shown in Table 4.8) at lower incident energies is observed. These disagreements with experimental data have not been observed in GEANT4 [33], due to the implementation of a specific low-energy electron transport model [34].

While Figure 4.5 shows that the reflection coefficients calculated from the GEANT3 simulation do not match experimental data for incident electron energies below 1.0 MeV, Figures 4.3 and 4.4 show that the transmission coefficients calculated from the GEANT3 simulation match experimental data excellently at incident electron energies of 500 keV. In addition, Figure 4.5 shows that the agreement with experimental reflection coefficients of and above 1.0 MeV is excellent. Referring once more to Figure 4.1, one can see that the number of δ rays with kinetic energies above 1.0 MeV produced by a 1.0 GeV incident pion is significant. Thus, for the purposes of this investigation, GEANT3 provides sufficient experimental agreement (at energies of and above 1.0 MeV) to validate its use. As GEANT3 is still the transport package of choice in the ALICE collaboration, it is of greater relevance to perform the investigation with GEANT3 than the more modern GEANT4. It would, however, be beneficial to implement a low-energy electron transport model

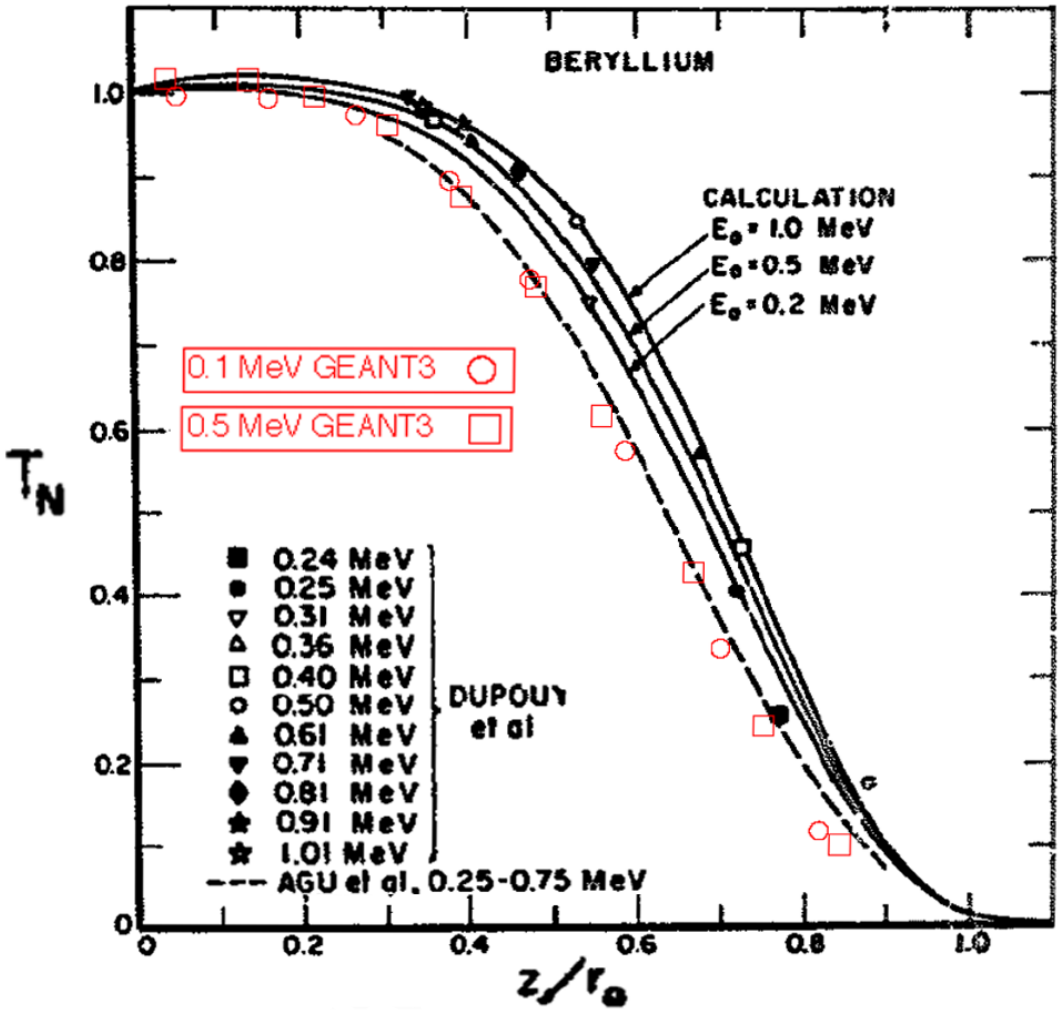

FIGURE 4.3: Transmission number coefficients for electrons traveling through beryllium at various energies. Points from the GEANT3 simulation are shown in red, while the solid line shows the results of the simulation performed in [32]. Systematically lower results than those in [32] are observed for larger z/r_0, but the results agree well with experimental results obtained by AGU et al. (dashed line).

(similar to that found in GEANT4, as detailed by [34]) into GEANT3, in order to ensure the accuracy of simulations across a larger kinetic energy range.

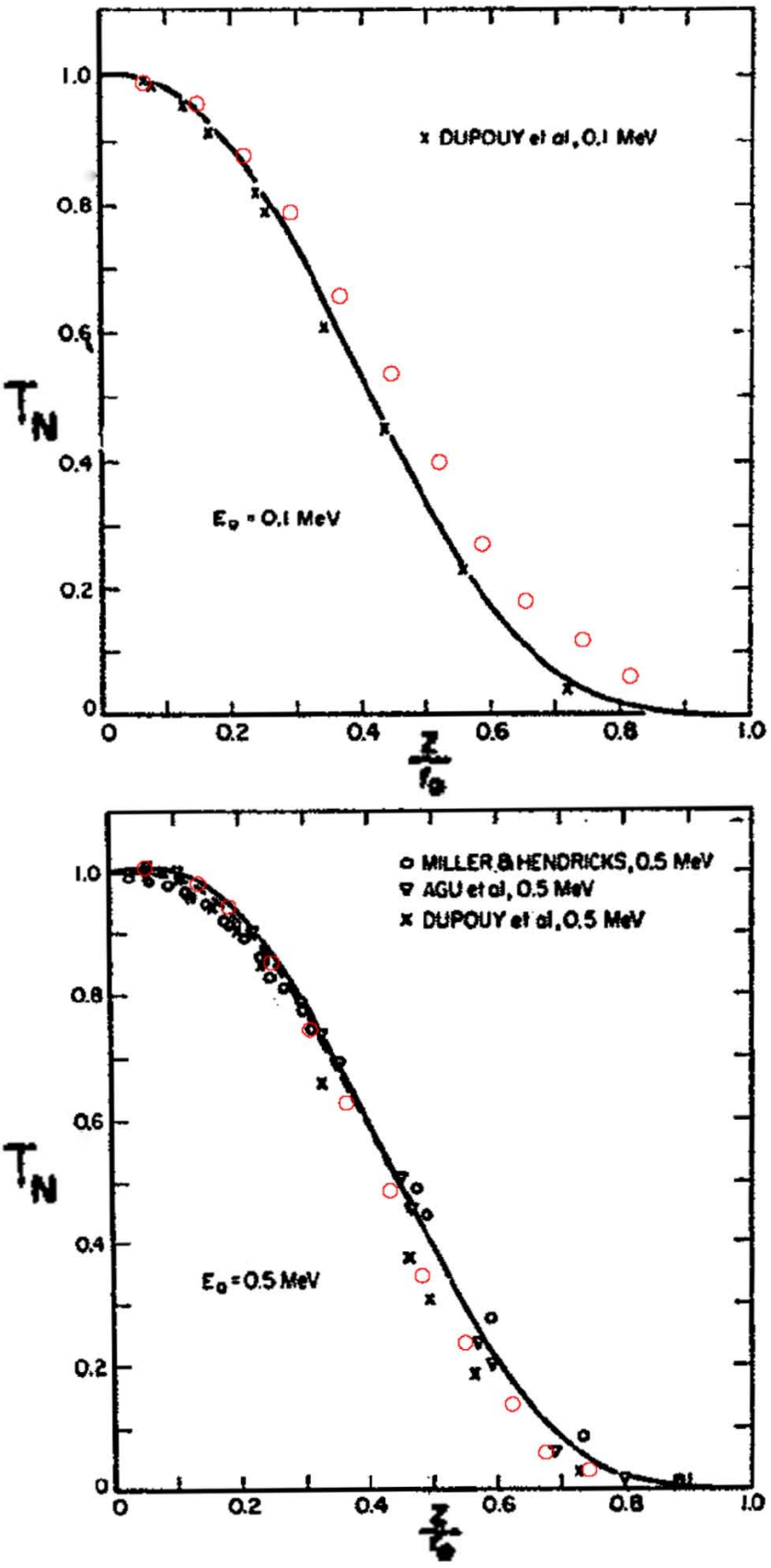

FIGURE 4.4: Transmission number coefficients for electrons travelling through aluminium at 100 keV (top) and 500 keV (bottom). Points from the GEANT3 simulation are shown in red, while the solid line shows the results of the simulation performed in [32]. Systematic deviation from the Monte-Carlo results in [32] is observed at 100 keV, while results at 500 keV closely match the experimental data referenced in [32].

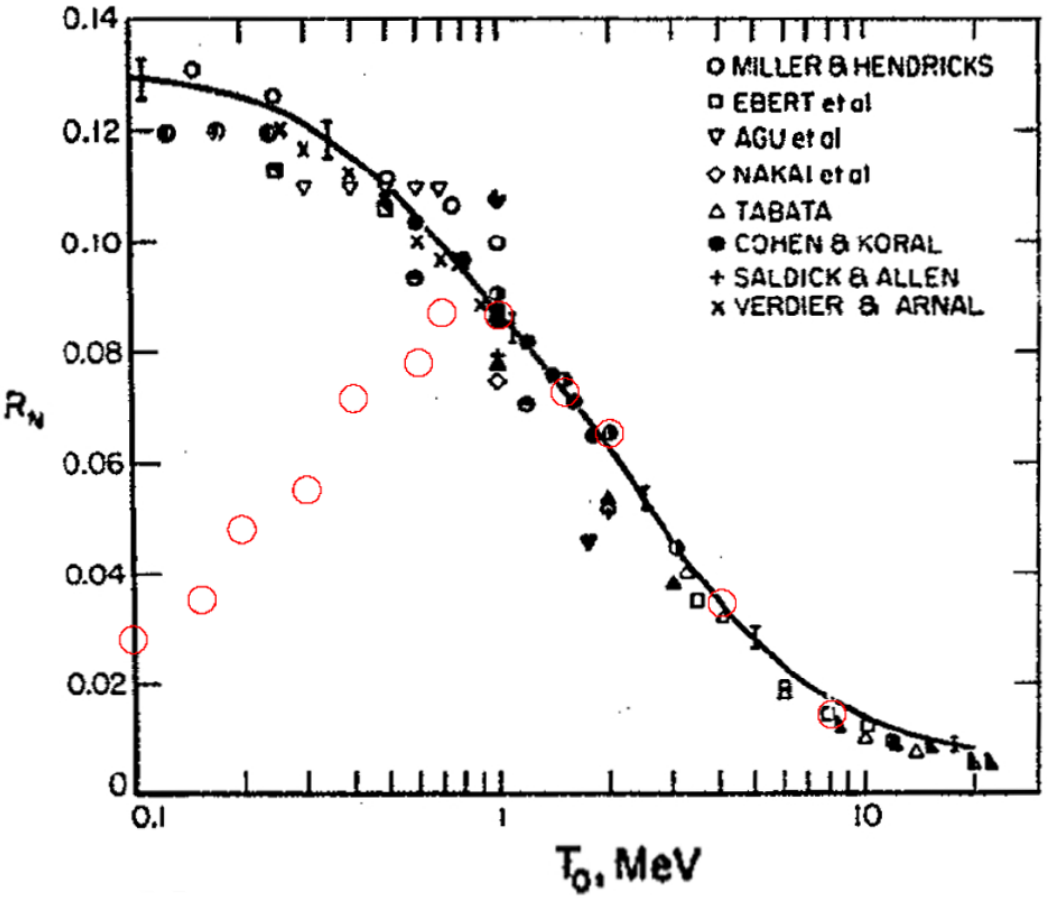

FIGURE 4.5: Reflection number coefficients for aluminium foils of saturation thickness at incident electron energies up to 8 MeV. Points from the GEANT3 simulation are shown in red, while the solid line shows the results of the simulation performed in [32]. While the values from the GEANT3 simulation match the experimental data very well above 1 MeV, they deviate significantly from the experimental values below 1 MeV.

TABLE 4.7: Transmission and reflection coefficients of electrons through beryllium and aluminium. Statistical errors are shown in brackets where the error is significant.

Foil thickness		Quantity	Incident energy (keV)				
(mils)	(mg/cm^2)	calculated	100	150	200	300	400
Beryllium							
2	9.40	T_N	0.682(2)	0.967(1)	0.997	1.004	1.005
3	14.10	T_N	0.121(1)	0.860(2)	0.972	1.002	1.006
5	23.50	T_N	0.000	0.312(2)	0.833(2)	0.985	1.002
2	9.40	R_N	0.005	0.009	0.007	0.003	0.002
3	14.10	R_N	0.004	0.009	0.010	0.006	0.003
5	23.50	R_N	0.005	0.008	0.012	0.012	0.007
2	9.40	T_E	0.368	0.761	0.869	0.934	0.957
3	14.10	T_E	0.034	0.554	0.774	0.895	0.933
5	23.50	T_E	0.000	0.109	0.516	0.802	0.880
2	9.40	R_E	0.002	0.004	0.004	0.002	0.001
3	14.10	R_E	0.002	0.004	0.005	0.003	0.002
5	23.50	R_E	0.002	0.004	0.006	0.007	0.004
Aluminium							
$\frac{1}{2}$	3.43	T_N	0.930(1)	0.992	0.997	1.002	1.003
1	6.86	T_N	0.667(3)	0.930(1)	0.981	0.999	1.003
2	13.72	T_N	0.108(2)	0.625(3)	0.867(2)	0.981	0.997
$\frac{1}{2}$	3.43	R_N	0.034(1)	0.012	0.008	0.003	0.003
1	6.86	R_N	0.030(1)	0.036(1)	0.020	0.008	0.004
2	13.72	R_N	0.026(1)	0.042(1)	0.052(1)	0.024(1)	0.011
$\frac{1}{2}$	3.43	T_E	0.794(1)	0.920	0.953	0.976	0.984
1	6.86	T_E	0.452(2)	0.783(1)	0.887(1)	0.947	0.967
2	13.72	T_E	0.043	0.399(2)	0.678(2)	0.870(1)	0.925
$\frac{1}{2}$	3.43	R_E	0.019	0.009	0.006	0.003	0.002
1	6.86	R_E	0.013	0.020	0.013	0.006	0.003
2	13.72	R_E	0.012	0.019	0.026	0.015	0.008

TABLE 4.8: Transmission and reflection coefficients of electrons through beryllium and aluminium obtained in [32].

Foil thickness (mils)	Foil thickness (mg/cm^2)	Quantity calculated	Incident energy (keV) 100	150	200	300	400
Beryllium							
2	9.40	T_N	0.730	0.980	0.992	1.005	1.005
3	14.10	T_N	0.205	0.902	0.978	1.003	1.006
5	23.50	T_N	0.000	0.471	0.881	0.996	1.005
2	9.40	R_N	0.018	0.013	0.006	0.003	0.002
3	14.10	R_N	0.018	0.017	0.012	0.005	0.003
5	23.50	R_N	0.018	0.017	0.018	0.009	0.005
2	9.40	T_E	0.407	0.782	0.876	0.938	0.959
3	14.10	T_E	0.068	0.606	0.795	0.902	0.936
5	23.50	T_E	0.000	0.197	0.573	0.822	0.889
2	9.40	R_E	0.009	0.007	0.004	0.001	0.001
3	14.10	R_E	0.009	0.008	0.006	0.003	0.001
5	23.50	R_E	0.009	0.008	0.008	0.004	0.002
Aluminium							
$\frac{1}{2}$	3.43	T_N	0.910	0.987	0.992	1.002	1.003
1	6.86	T_N	0.602	0.918	0.968	0.997	1.004
2	13.72	T_N	0.046	0.601	0.845	0.979	0.996
$\frac{1}{2}$	3.43	R_N	0.076	0.018	0.008	0.005	0.002
1	6.86	R_N	0.124	0.070	0.031	0.010	0.005
2	13.72	R_N	0.125	0.118	0.100	0.030	0.014
$\frac{1}{2}$	3.43	T_E	0.766	0.918	0.955	0.978	0.987
1	6.86	T_E	0.393	0.766	0.880	0.949	0.969
2	13.72	T_E	0.017	0.384	0.660	0.873	0.926
$\frac{1}{2}$	3.43	R_E	0.050	0.014	0.005	0.002	0.000
1	6.86	R_E	0.071	0.045	0.022	0.007	0.002
2	13.72	R_E	0.072	0.066	0.058	0.021	0.009

Chapter 5

Simulation of a Simple Pixel Detector

5.1 Introduction

To investigate the effect of δ rays on the impact parameter measurements in the ITS, a simulation of a simple pixel detector, modelled on the ITS SPD, was performed using the GEANT3 package. For comparison, the simulation was also performed on an altered geometry, modelled on the proposed update to the SPD. The layout of the geometries based on the original and updated SPD geometries, henceforth referred to as the simplified SPD (sSPD) and simplified updated SPD (uSPD) geometries respectively, are shown in Figures 5.1 and 5.2 respectively, while the various parameters of these geometries are compared in Table 5.1. The overall layout of pixel modules for the sSPD and uSPD geometries are shown in Figures 5.3 and Figures 5.4 respectively. In order to simplify the simulation setup, only one pixel module was simulated for each geometry. Charged pions of a specific momentum $\mathbf{p}$ were fired isotropically from the beam line, with varying polar and azimuthal angles θ and ϕ respectively[1]. θ was varied across events between values of 0 and $\theta_{\text{max}} = 0.3$ radians, while ϕ was varied between values of 0 and $\phi_{\text{max}} = 0.1$ radians in order to investigate the behaviour of incident particles across a larger area of the pixel module, rather than just the centre. The incident particle energies were taken as values between 0.3 GeV and 2.0 GeV so as to investigate the impact

[1]The polar angle θ is taken as the angle between the particle momentum and the normal of the pixel module, perpendicular to the beam pipe, while the azimuthal angle ϕ is defined as the angle giving rotations about the beam axis.

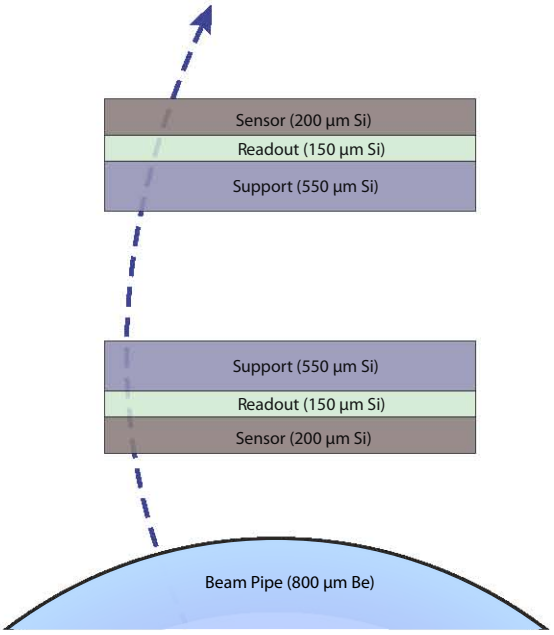

FIGURE 5.1: Schematic diagram of the simplified pixel detector setup (sSPD), with measurements based on the ITS pixel detectors. In the first layer, the sensor is positioned radially inward of the readout chip and support structure, while in the second layer the order is reversed.

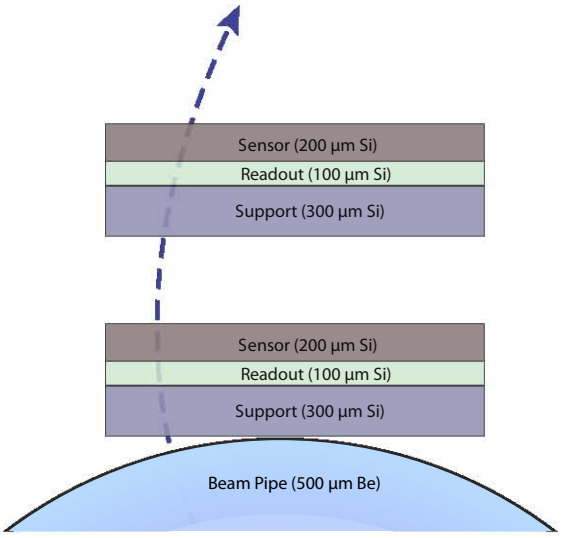

FIGURE 5.2: Schematic diagram of the simplified updated pixel detector setup (uSPD), with measurements based on the proposed update to the ITS pixel detectors, where the first layer is positioned against the beam pipe.

parameter resolution's dependence on primary particle momentum. The particles were transported through a 5.0 kG magnetic field directed along the beam axis, resulting in helical tracks.

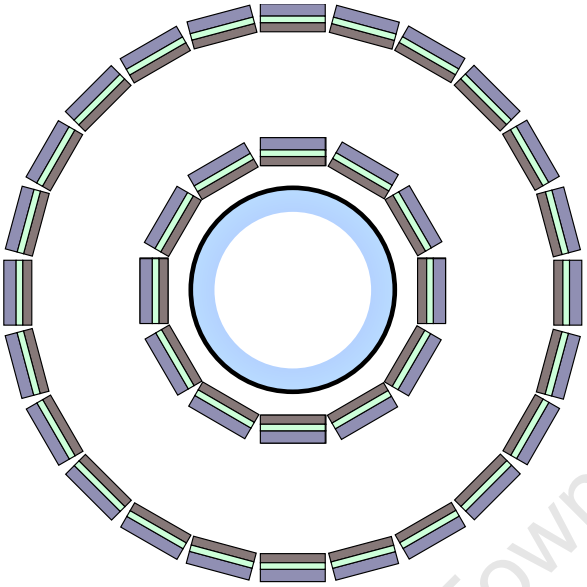

FIGURE 5.3: Positioning of the simplified pixel detector elements (sSPD), with measurements based on the ITS pixel detectors. There is a small dead zone between modules which is not present in the ALICE detector due to the actual SPD's azimuthal arrangement, shown in Figure 3.5.

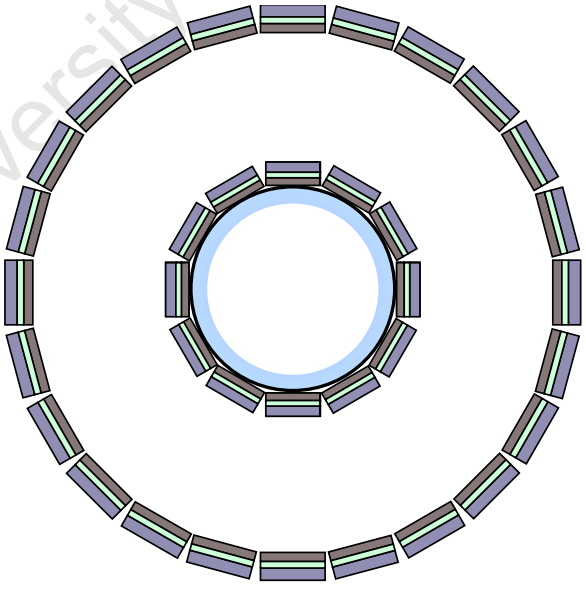

FIGURE 5.4: Positioning of the simplified updated pixel detector elements (uSPD), with measurements based on the proposed update to the ITS pixel detectors, with the inner layer positioned against the beam pipe, which has a reduced radius and thickness.

TABLE 5.1: Table of various parameters of the simulation setup for geometry based on the ITS SPD dimensions (sSPD), as well as those based on the proposed update (uSPD).

Parameter	Unit	sSPD Geometry	uSPD Geometry
Beam Pipe Radius	cm	2.92	2.00
Beam Pipe Thickness	μm	800	500
Inner Layer Radius	cm	3.90	2.05
Outer Layer Radius	cm	7.60	4.00
Pixel Thickness	μm	200	200
Pixel Width ($r\phi$)	μm	50	20
Pixel Length (z)	μm	425	300
Readout Thickness	μm	150	100
Support Thickness	μm	550	300

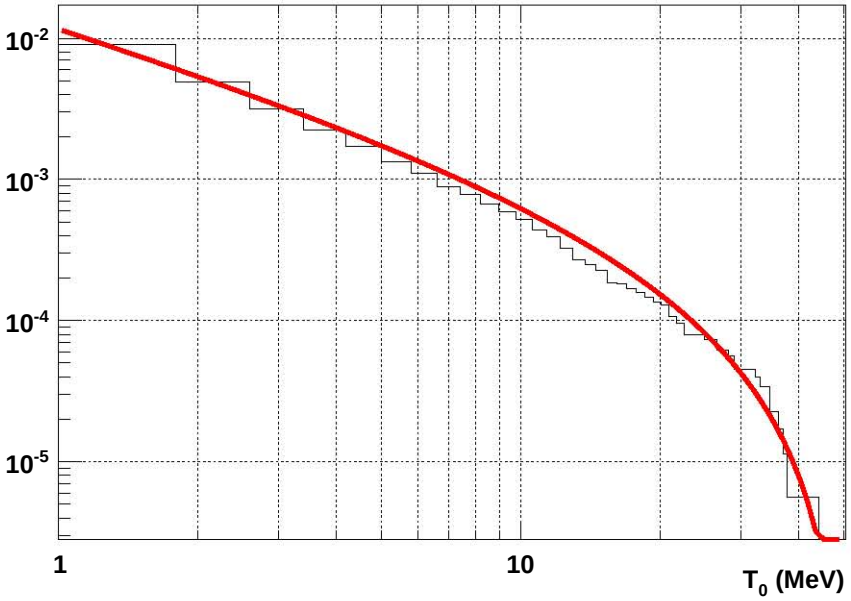

FIGURE 5.5: The red line shows the energy spectrum of δ rays produced in the 800 μm beam pipe of the sSPD simulation, alongside the theoretical prediction, obtained by integrating Equation 4.6 from T_0 to $T_{\max}$. The histogram shows the average number of δ rays with kinetic energy $T > T_0$, produced by an incident pion of momentum 1.0 GeV/c, travelling through the beryllium beam pipe.

The energy spectra of δ rays produced in the beam pipe of the sSPD and uSPD simulations are shown in Figures 5.5 and Figures 5.6 respectively, alongside the theoretical prediction following Equation 4.6. Also shown in Figures 5.7 and 5.8 are the energy spectra of δ rays produced in the inner layer of the sSPD and uSPD geometries respectively.

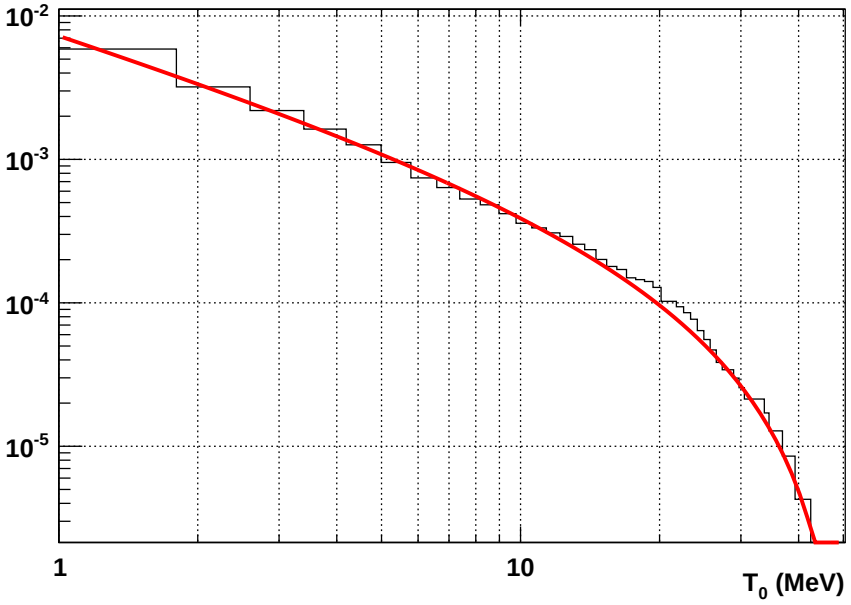

FIGURE 5.6: The red line shows the energy spectrum of δ rays produced in the 500 μm beam pipe of the uSPD simulation by an incident pion of momentum 1.0 GeV/c. In comparison with Figure 5.5, fewer δ rays are produced due to the thinner beam pipe.

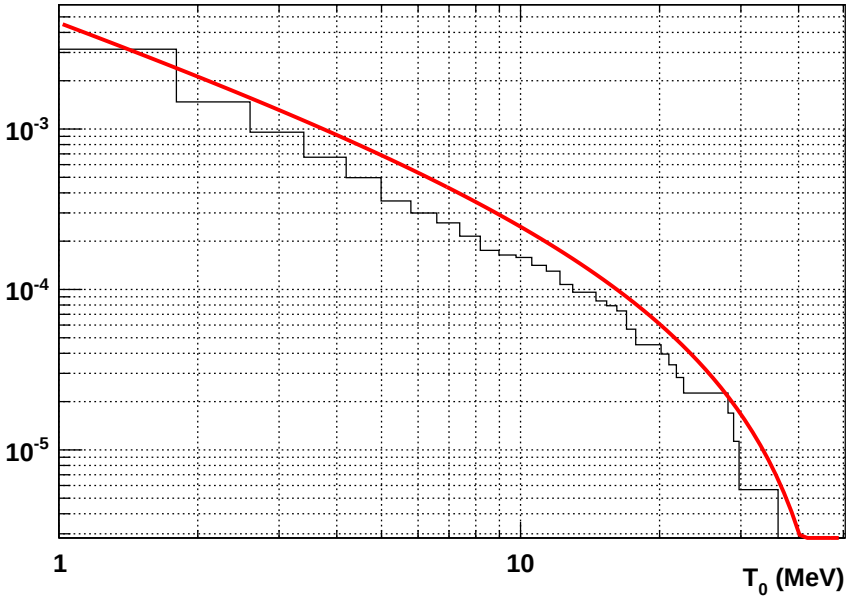

FIGURE 5.7: The red line shows the energy spectrum of δ rays produced in the inner layer of the sSPD simulation by an incident pion of momentum 1.0 GeV/c. The simulation's spectrum does not differ significantly from the theoretical prediction, as described by Equation 4.6.

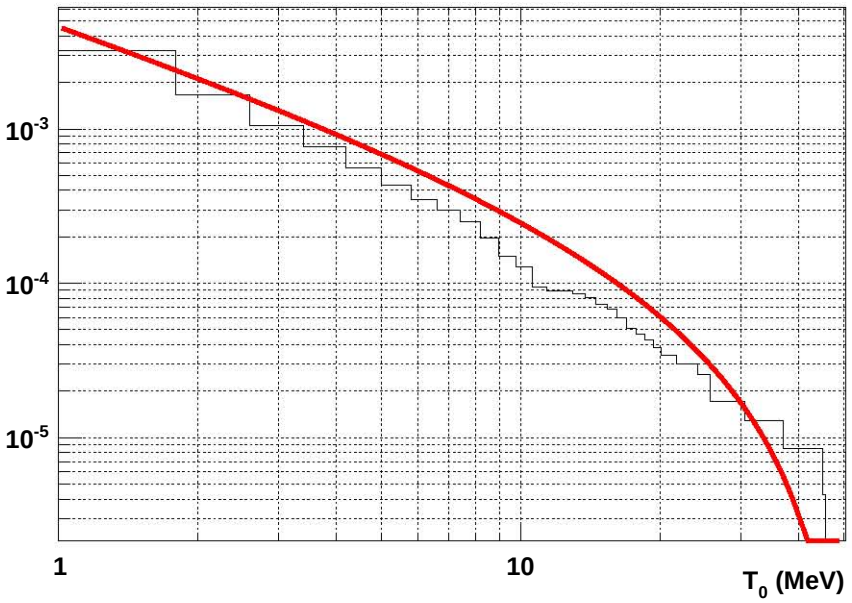

FIGURE 5.8: The red line shows the energy spectrum of δ rays produced in the inner layer of the uSPD simulation by an incident pion of momentum 1.0 GeV/c. As the pixel thicknesses are the same, the spectrum does not differ significantly from that of the sSPD simulation, shown in Figure 5.7. The deviation at the higher end of the spectrum can be assumed to be purely statistical, as the frequency of δ rays produced at these energies is too low for the number of simulated events to produce an accurate bin.

5.2 Calculation of Pion Hit Positions

As particles travel through the detector, they deposit energy via continuous energy loss, detailed in Section 4.2.1. The energy lost during each step in each particle's transport is recorded. At the end of an event, the total energy deposited in each pixel is calculated and pixel hits are recorded.

Acceptance criteria for pixel hits

Two factors are considered when calculating the acceptance of a pixel hit. Firstly, the total energy deposited in the pixel, E_T, must be above an acceptance threshold energy, $E_{\min}$, which for this simulation was chosen to be 2 keV, to match the current threshold energy of the ALICE ITS pixel detectors [17]. Secondly, only hits contiguous[2] to at least one pion hit are accepted (In the ITS, this information would be provided by the SDDs and SSDs). The distributions of pixel hits on the inner layers of the sSPD and uSPD geometry are shown in Figures 5.9 and 5.10 respectively. One can see that the number of δ rays does not vary appreciably as the momentum of the incident particle is increased. One can verify that this is the expected behaviour by integrating Equation 4.6 from the δ ray minimum threshold energy $T_{\min}$=2.0 keV to the maximum δ ray energy, which varies with incident particle energy according to Equation 4.2. The expected number of δ rays as a function of incident particle momentum p is then related to $T_{\max}(p)$ and $T_{\min}$:

$$\langle N(p)\rangle \sim \int_{T_{\min}}^{T_{\max}(p)} \frac{dN}{dTdx} dT \tag{5.1}$$

$$\sim \frac{T_{\max}(p) - T_{\min}}{T_{\min}T_{\max}(p)} + \frac{\beta^2}{T_{\max}(p)} \ln \frac{T_{\min}}{T_{\max}(p)}. \tag{5.2}$$

For an incident pion, $T_{\max}$ (2.0 GeV/c) = 190.0 MeV, while $T_{\max}$ (0.3 GeV/c) = 4.6 MeV. Substituting these values into Equation 5.2 shows that the relative difference between $\langle N(2.0 \text{ GeV}/c)\rangle$ and $\langle N(0.3 \text{ GeV}/c)\rangle$ is less than 0.5%.

[2]Two hits are contiguous if there exists a path between them, along which each pixel has also been hit.

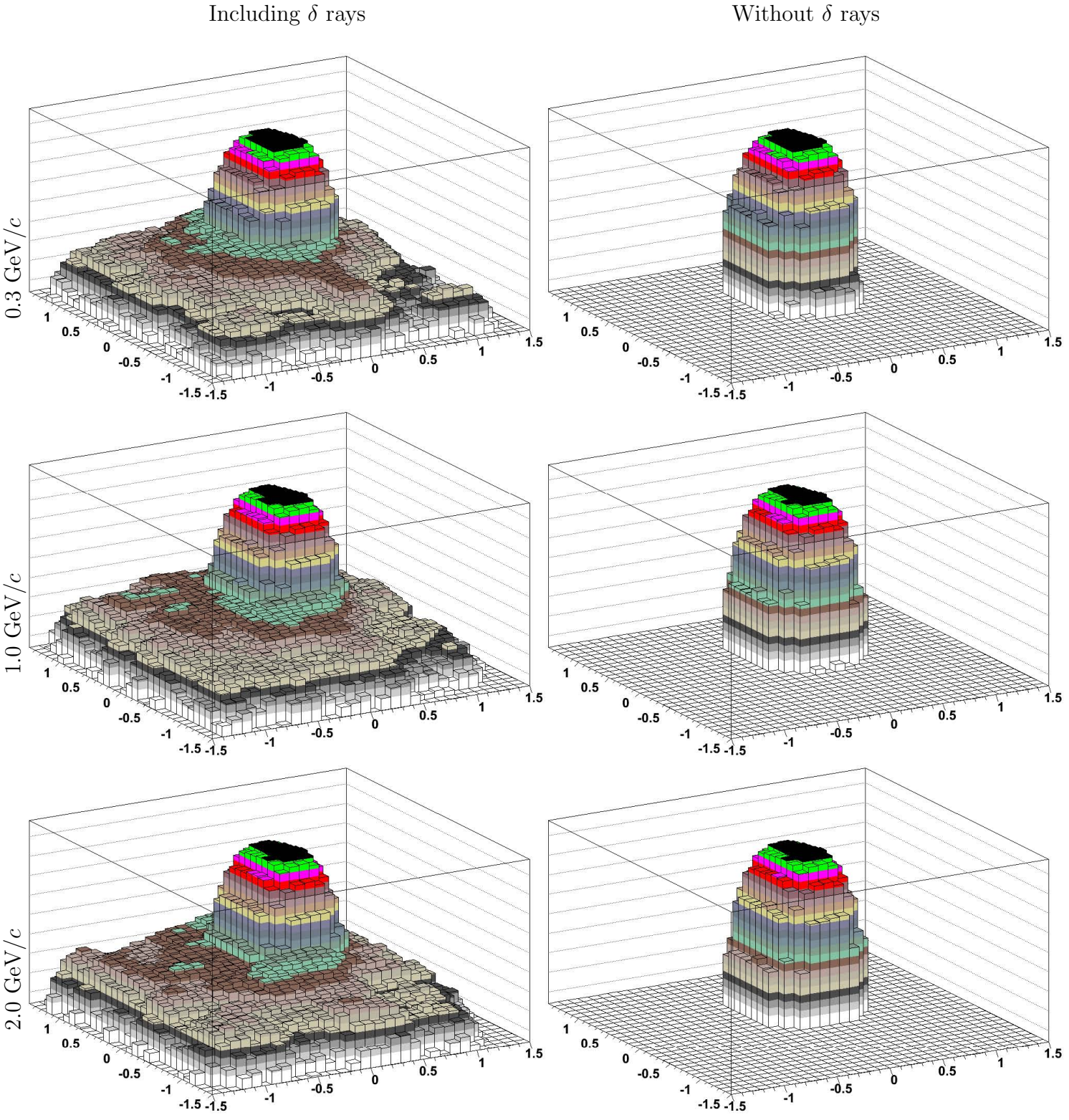

FIGURE 5.9: Pixel hit distribution on one module of the inner layer of the sSPD simulation, for various incident pion momenta, shown both with and without δ rays. 300 000 events were simulated for each pion momentum, with isotropic emission, as described in Section 5.1. Units shown are in cm, with the number of hits shown on the vertical axis. One can see that the inclusion of δ ray hits creates a noisy distribution.

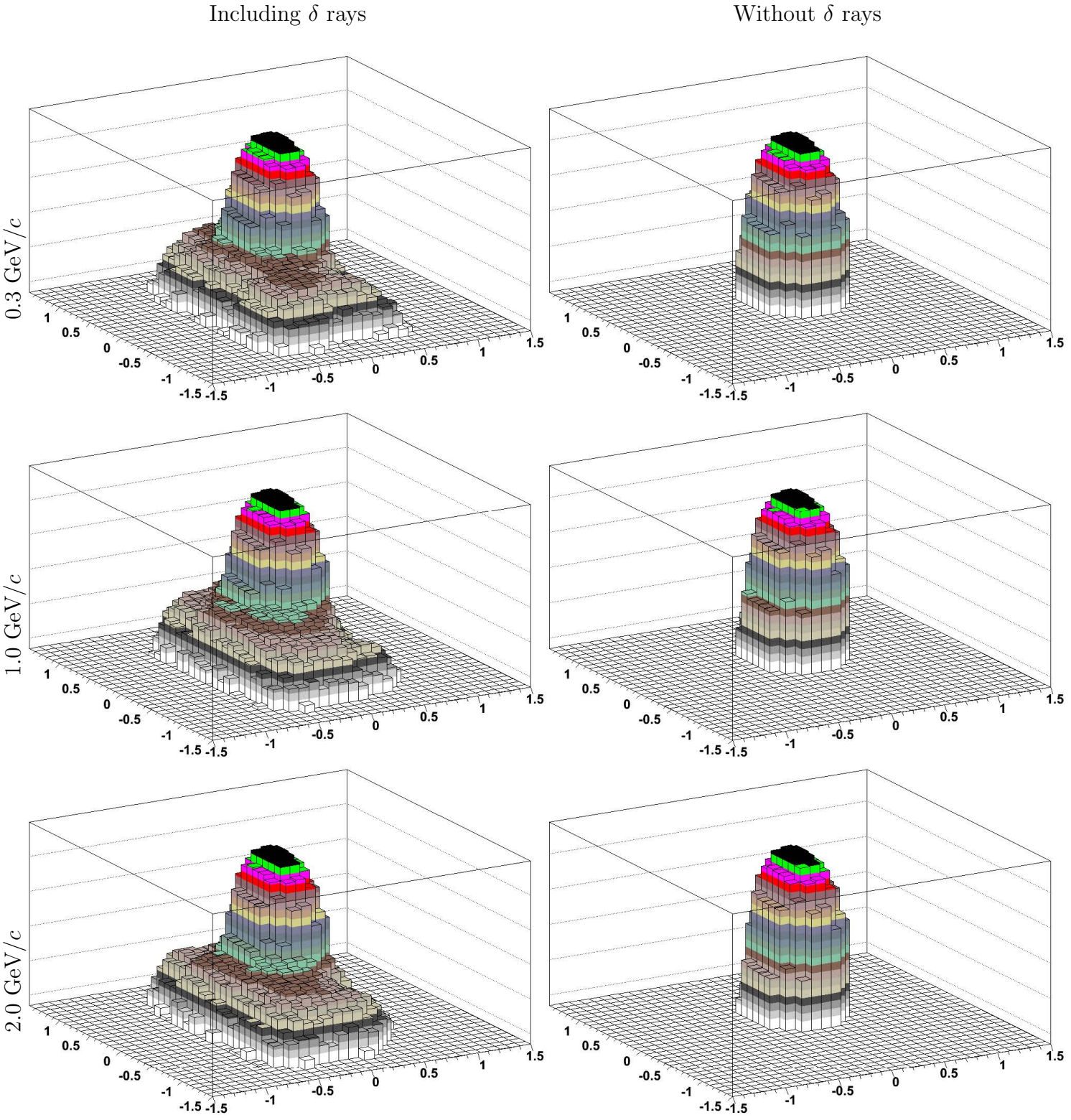

FIGURE 5.10: Pixel hit distribution on one module of the inner layer of the uSPD simulation, for various incident pion momenta, shown both with and without δ rays. 300 000 events were again simulated for each pion momentum, with isotropic emission. For the same number of pixels per module, the reduced pixel size leads to a smaller hit distribution when compared to Figure 5.9.

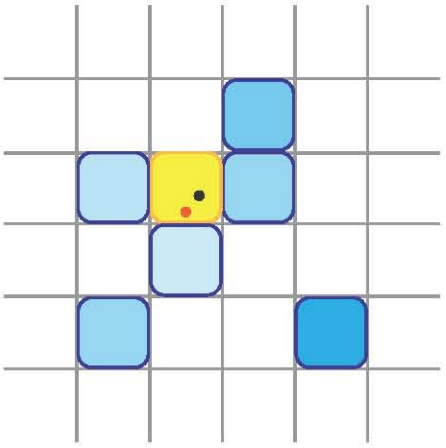

FIGURE 5.11: Example of pixel hits from a single event. The pion hit is shown in yellow, while δ ray hits are shown in blue, with the intensity of shading representing the relative energy deposited in each pixel. The rightmost δ ray hit is discarded in the calculation of the average hit position, as it is not contiguous to a pion hit. The unweighted mean position is represented by the red circle, while the weighted mean position is represented by the black circle. In the absence of all δ rays, the hit position would be simply taken as the centre of the pixel that was hit by the incident pion.

Calculating the average hit position

Lowering E_{min} has the effect of accepting a large number of low energy δ ray hits. To investigate the effect of these low energy hits, two methods for calculating the average hit positions for each layer were used: both an unweighted (arithmetic) mean of all hits on a layer as well as a weighted mean, weighted by the energy deposited E_T, as shown in Figure 5.11. By comparing the results obtained with these two definitions of the average hit position, one can investigate the effect of the abundant low energy δ rays on the impact parameter. In a more realistic situation, a Gaussian smearing of the energy deposits across neighbouring pixels would be performed, in order to simulate the energy diffusion. This is detailed in [35].

5.3 Calculation of the Impact Parameter from Pion hits

The impact parameter d_0 can be reconstructed for each tracked pion from its associated pixel hits in the two SPD layers, originating from both the pion's energy

deposits itself (primary hits), as well as from δ ray energy deposits (secondary hits). An accurate measurement of the impact parameter allows one to judge the likelihood of a track originating from a secondary decay vertex, such as that of a charm or bottom quark.

Calculating the $r\phi$ projection of the impact parameter for single pion tracks

In the absence of a magnetic field, the impact parameter d_0 of a track can be defined as the distance of closest approach from the track to the primary vertex position $\mathbf{P_0}$. In the case of a pion travelling through two parallel planes, hitting the first plane at $\mathbf{P_1}$ and the second at $\mathbf{P_2}$, the track can be determined by simply extending the line from $\mathbf{P_2}$ to $\mathbf{P_1}$. The distance of closest approach is thus given as

$$d_0 = \frac{|(\mathbf{P_0} - \mathbf{P_1}) \times (\mathbf{P_0} - \mathbf{P_2})|}{|\mathbf{P_1} - \mathbf{P_2}|}. \tag{5.3}$$

As the dimensions of the individual pixels in each layer are different in the $r\phi$ and zn plane[3], it is useful to calculate the projection of d_0 in both the $r\phi$ and zn planes, $d_0(r\phi)$ and $d_0(zn)$ respectively. One can extend the definition of $d_0(r\phi)$ to also give the orientation of the pion track, relative to the primary vertex $\mathbf{P_0}$. In this case, $d_0(r\phi)$ is given by

$$d_0(r\phi) = \frac{([\mathbf{P'_0} - \mathbf{P'_1}] \times [\mathbf{P'_0} - \mathbf{P'_2}]) \cdot \hat{\mathbf{z}}}{|\mathbf{P'_1} - \mathbf{P'_2}|}, \tag{5.4}$$

where the prime indicates the projection in the $r\phi$ plane. Figure 5.12 shows $d_0(r\phi)$ in relation to $\mathbf{P'_0}$, $\mathbf{P'_1}$ and $\mathbf{P'_2}$ (the position vectors in the $r\phi$ plane).

[3]The $r\phi$ plane is defined by the unit vectors $\hat{r}$ and $\hat{\phi}$, while the zn plane is defined by the beam direction and the normal of the pixel module, $\hat{n}$.

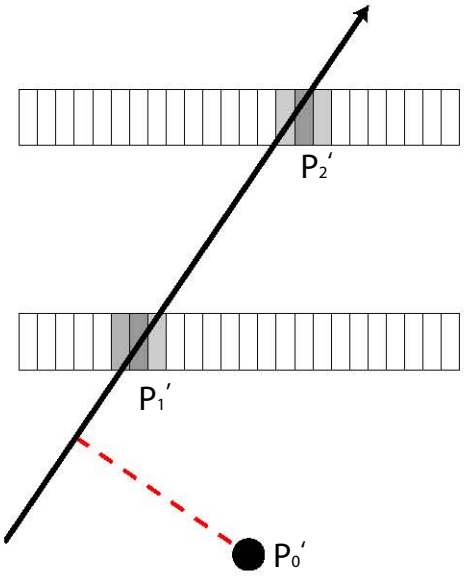

FIGURE 5.12: The impact parameter projection $d_0(r\phi)$ is shown as the dashed line, perpendicular to the extension of the line drawn from $\mathbf{P'_2}$ to $\mathbf{P'_1}$. By Equation 5.4, tracks passing to the left of $\mathbf{P'_0}$ will have $d_0(r\phi) < 0$ while those passing to the right of $\mathbf{P'_0}$ will have $d_0(r\phi) > 0$.

When travelling in the presence of a uniform magnetic field of strength B, charged particle tracks become helices, as shown in Figure 5.13. From the momentum of the particle, one can calculate the radius of curvature of the track:

$$R = \frac{p_T}{0.3B}, \tag{5.5}$$

with B in Teslas, p_T in units of GeV/c and R in metres. One can use this to find the centre of curvature $\mathbf{P'_C}$, as

$$|\mathbf{P'_1} - \mathbf{P'_C}|^2 = |\mathbf{P'_2} - \mathbf{P'_C}|^2 = R^2. \tag{5.6}$$

One can then define the $r\phi$ projection of the impact parameter as

$$d_0(r\phi) = q\left(R - \sqrt{|\mathbf{P'_C} - \mathbf{P'_0}|^2}\right), \tag{5.7}$$

where q is the sign of the particle's charge. This does not take into account the effect of energy loss in the pixel detectors on the radius of curvature, which can be estimated by Equation 4.1. In this study, pions were tracked from the primary

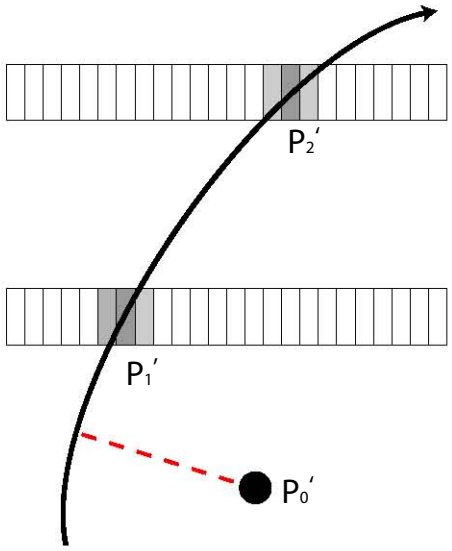

FIGURE 5.13: The impact parameter projection $d_0(r\phi)$ of a charged particle in a uniform magnetic field is shown as the dashed line, perpendicular to the extension of the curve drawn from $\mathbf{P'_2}$ to $\mathbf{P'_1}$. Tracks with radius of curvature larger than the distance from $\mathbf{P'_0}$ to the centre of curvature $\mathbf{P'_C}$ will have $d_0(r\phi) > 0$.

vertex, $\mathbf{P_0}$, through the two layers of SPDs. In the absence of multiple scattering, energy loss and δ ray production, $\langle d_0(r\phi)\rangle$ would naturally be zero. Table 5.2 shows $\langle d_0(r\phi)\rangle$ for configurations with and without magnetic field, with all relevant physical effects (i.e energy loss, multiple scattering and δ ray production) included. One can see that values of $\langle d_0(r\phi)\rangle$ are low for all simulation configurations, showing that the impact parameter algorithms with and without magnetic field (described by Equation 5.7 and 5.4 respectively) do not lead to a significant bias. The systematic deviation from $\langle d_0(r\phi)\rangle = 0$ observed in each simulation is likely due to the alignment of the geometry of the individual pixels. Relative to the spatial resolution obtained by the actual ITS pixel detectors [23], one can assume that the results are consistent with $\langle d_0(r\phi)\rangle = 0$.

TABLE 5.2: Table of mean values of impact parameter projection $d_0(r\phi)$ for sSPD and uSPD geometries, with and without magnetic field, for various incident pion momenta.

p (GeV/c)	$d_0(r\phi)$ (μm)			
	sSPD	sSPD ($B = 0$)	uSPD	uSPD ($B = 0$)
0.3	0.47±0.55	0.84±0.54	0.24±0.20	0.19±0.20
1.0	0.27±0.17	0.20±0.17	0.00±0.06	0.03±0.06
2.0	0.26±0.10	0.19±0.10	0.00±0.03	0.02±0.03

Figures 5.14 and 5.15 show impact parameter distributions for the sSPD simulation and the uSPD simulation respectively, for various incident pion momenta. One can see that an increase in incident particle momentum leads to a sharper peak at $d_0(r\phi) = 0$. The exclusion of δ rays lowers the distribution tail, which leads to an improved impact parameter resolution. A comparison of the sSPD and uSPD simulation shows that the peaks are consistently sharper in the latter, due primarily to the decreased material budget.

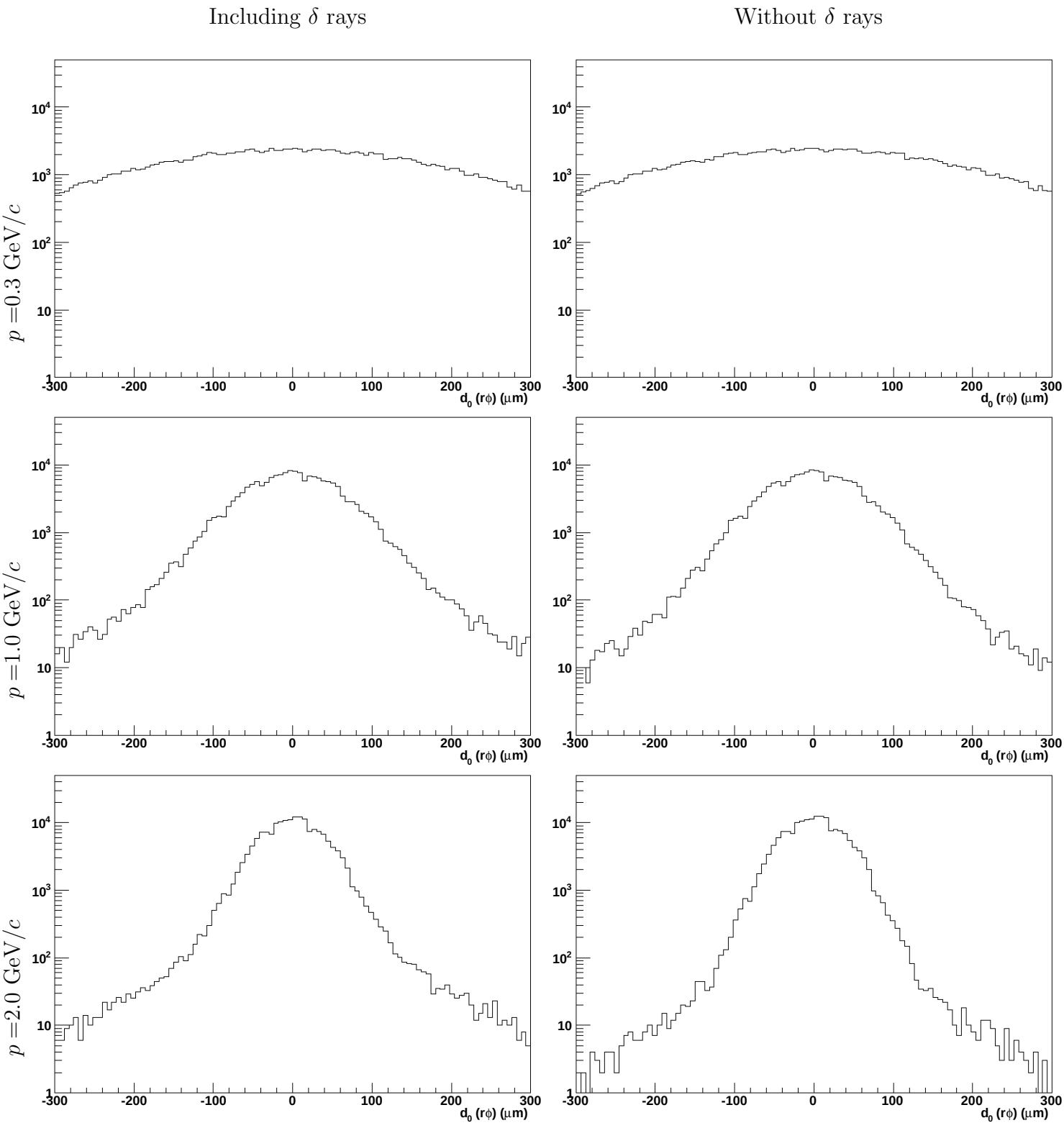

FIGURE 5.14: Distribution of impact parameter projection $d_0(r\phi)$ for the sSPD simulation of 300 000 events for each value of p, with a 5.0 kG magnetic field enabled.

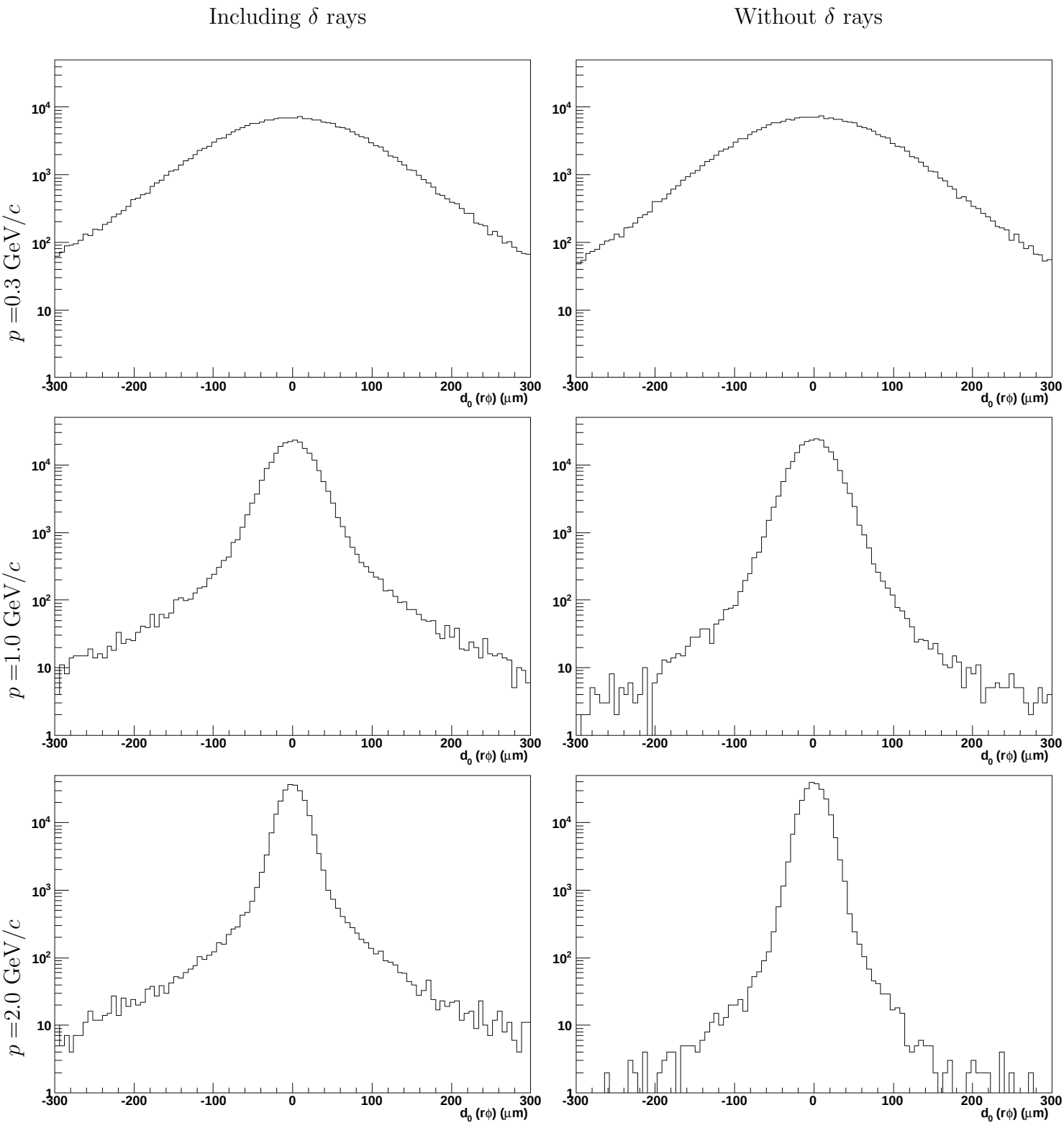

FIGURE 5.15: Distribution of impact parameter projection $d_0(r\phi)$ for the uSPD simulation of 300 000 events for each value of p, with a 5.0 kG magnetic field enabled.

5.4 Impact Parameter Resolution

Figure 5.16 shows a comparison between the impact parameter resolution of the two simulation setups as a function of incident pion momentum, with and without δ rays. One can see that the effect of δ rays becomes more significant at higher momenta, as more energetic δ rays are created. One can see that the uSPD simulation has an improved resolution over the entire momentum range. However, the effect of δ rays is more pronounced than in the sSPD simulation. Two possible explanations can be given:

- A number of δ rays are produced in the beam pipe itself. These δ rays travel through the beam pipe and may go on to hit the first layer. If the first layer is constructed directly against the beam pipe, some of these δ rays may create hits in the region of the incident pion's hits. This would adversely affect the impact parameter resolution. The uSPD geometry places the first layer directly against the beam pipe and would thus be susceptible to this effect, while the distance between the beam pipe and the first layer in the sSPD geometry would ensure that most δ rays originating in the beam pipe would not pass through a region contiguous with the pion's hits.
- Most δ rays travel only a very small distance inside the detector medium. The size of the pixels will determine the probability of a δ ray crossing over to an adjacent pixel and generating an additional hit. The uSPD geometry has a smaller pixel size, meaning an additional number of δ ray hits would be generated, adversely affecting the impact parameter resolution.

In order to determine which of these explanations is correct, or whether it is due to a combination of the two, a simulation was performed with a 10 μm beam pipe, ensuring that the contribution of δ rays created in the beam pipe is negligible. Figure 5.17 shows the resulting graph. One can see that the effect of δ rays is still more pronounced in the uSPD simulation, suggesting that the second explanation is the correct one. Comparing the results without δ rays in Figure 5.17 with those in Figure 5.16 shows that the effect of deflections of the incident pion within the beam pipe is exaggerated at lower momenta. At momenta above 1 GeV/c, the contribution is less than 5%.

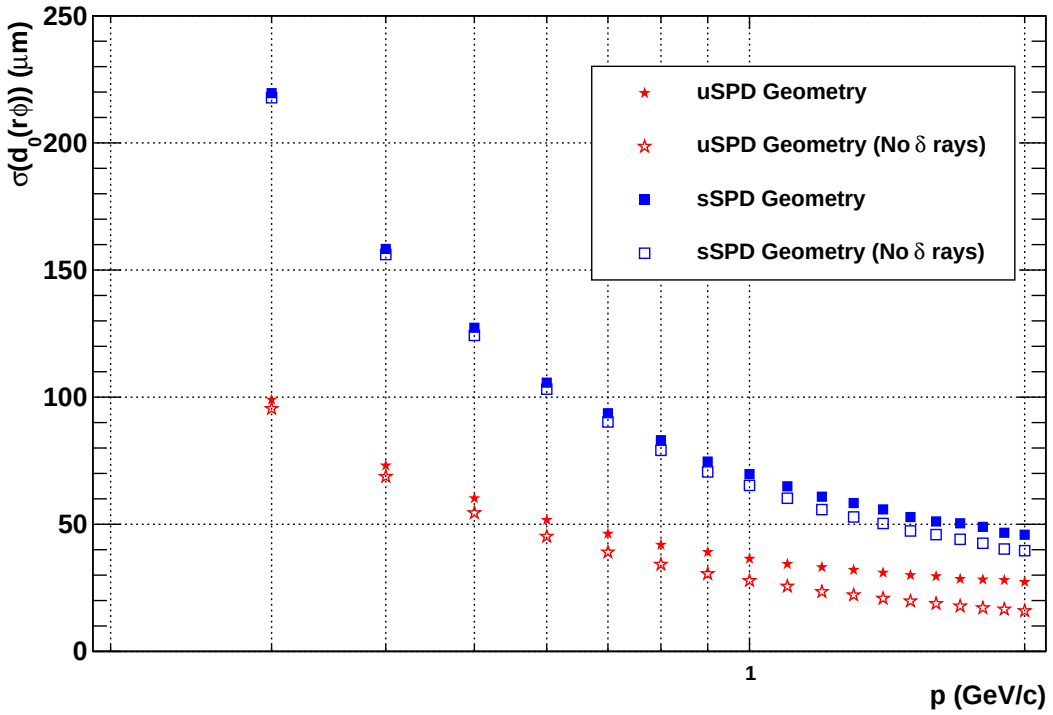

FIGURE 5.16: Resolution of impact parameter projection $d_0(r\phi)$ as a function of incident pion momentum p.

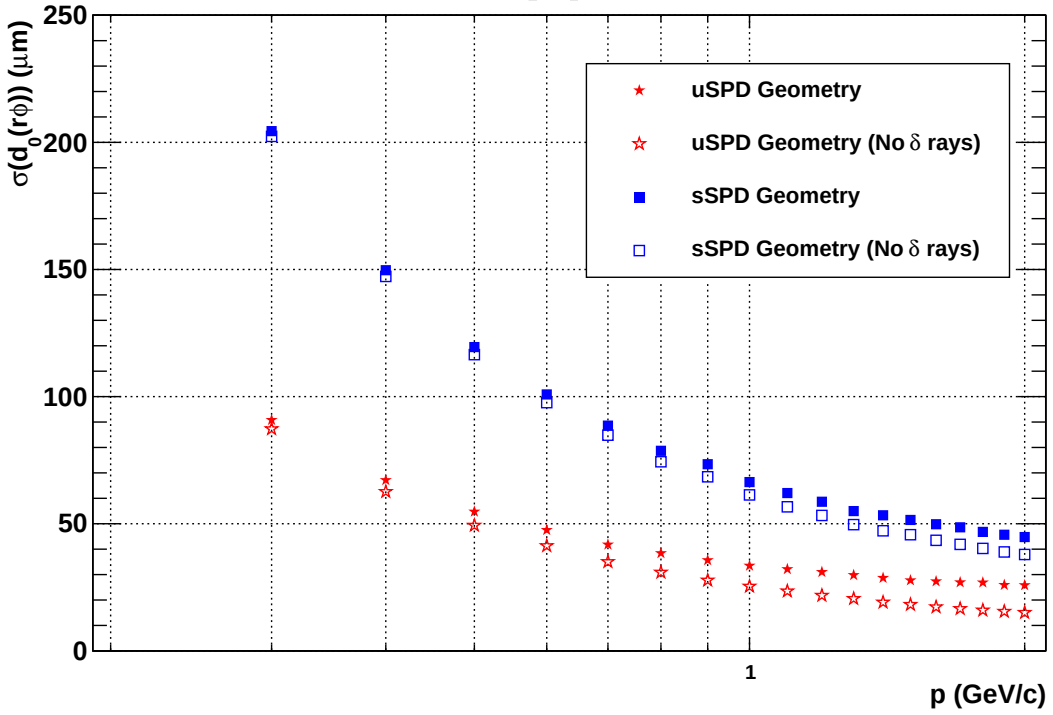

FIGURE 5.17: Resolution of impact parameter projection $d_0(r\phi)$ as a function of incident pion momentum p, simulated with a negligibly thin beam pipe.

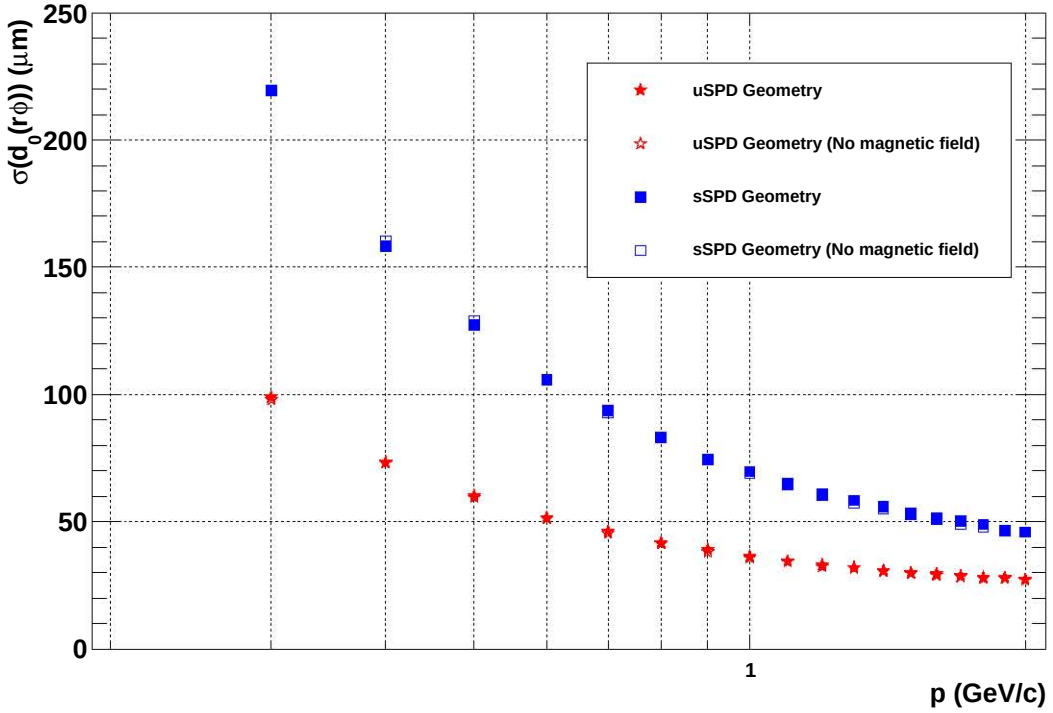

FIGURE 5.18: Resolution of impact parameter projection $d_0(r\phi)$ as a function of incident pion momentum p, with and without the presence of a magnetic field.

Figure 5.18 shows the impact parameter resolution with and without a simulated magnetic field. The algorithms used to determine $d_0(r\phi)$ in each case are different, as they stem from Equations 5.7 and 5.4 respectively. One can see that the magnetic field does not affect the impact parameter resolution significantly.

Figure 5.19 shows the impact parameter resolution with and without weighting in the average hit calculation, as described in Section 5.2. No significant improvement to the impact parameter resolution is observed. At higher momenta, the weighted average produces a slightly improved resolution in the uSPD simulation. This is due to the increased energy deposits from the incident pion, which are then biased above lower energy δ ray energy deposits in the calculation of the average hit position.

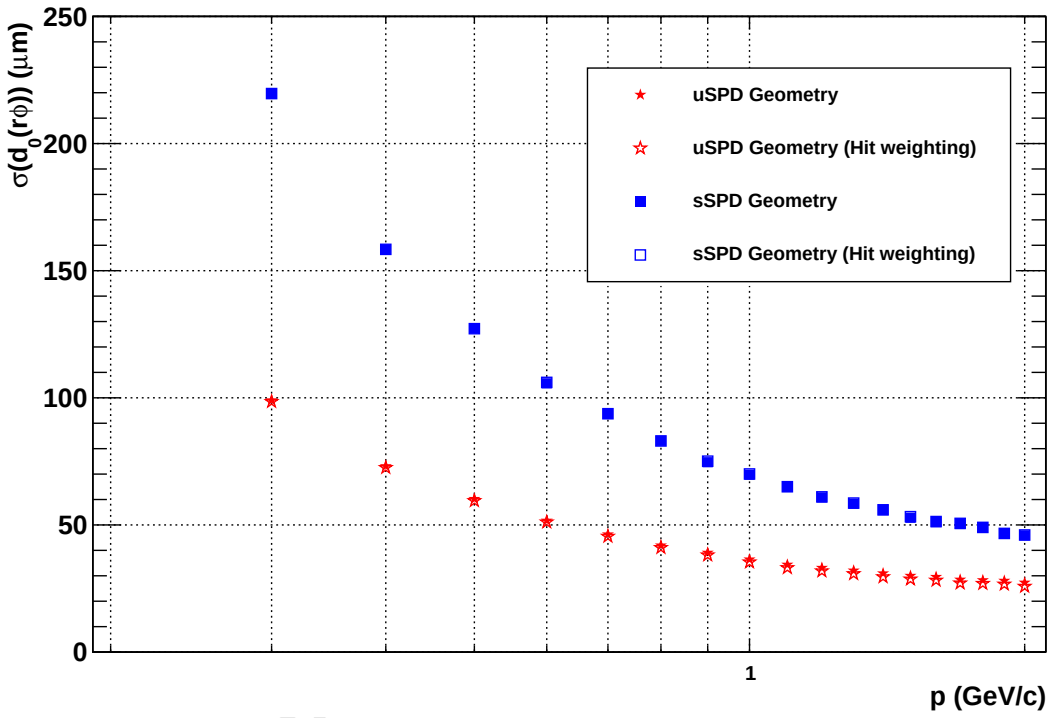

FIGURE 5.19: Resolution of impact parameter projection $d_0(r\phi)$ as a function of incident pion momentum p, using unweighted and weighted hit position calculations.

Chapter 6

Conclusion

The purpose of this study was to investigate the effect of δ rays, originating in the beam pipe and pixel detectors of the ITS, on the impact parameter resolution, in order to highlight what modifications could be made to improve the detection of heavy decay vertices, for which impact parameter is a vital observable. With the aid of a simulation utilising the GEANT3 transport package, in which a simplified model of the ITS pixel detector was constructed, this study has shown that the effect of δ rays on impact parameter resolution is significant, and becomes more prominent with increasing incident particle momentum.

Comparing the results of Figure 5.16 to those shown in [36], one finds that the calculations of impact parameter resolution obtained in this study's sSPD (ITS-based geometry) simulation closely match those measured by the ALICE collaboration during the first year of proton-proton collisions. While this study's simulation is a simplified model of the underlying physics, it highlights the benefits of modifying the geometry of the ITS in future upgrades in order to improve the impact parameter resolution and hence more consistently detect rare heavy decay vertices. When compared to the sSPD geometry, the uSPD (updated ITS-based) geometry shows an improvement of 48% in impact parameter resolution for a pion with 1.0 GeV/c incident momentum. However, the simulation shows that the effect of δ rays will be exaggerated under the updated geometry. For a pion with incident momentum of 1.0 GeV/c, the inclusion of δ rays in the calculation of the impact parameter leads to an 11% degradation in resolution in the case of the uSPD geometry, but only a 2% degradation in the case of the sSPD geometry. By adjusting the simulation to include an artificially thin beam pipe, we have shown that, contrary to

initial assumptions that the proximity to the beam pipe in the proposed geometry would be the cause of this exaggeration, the primary reason for this exaggeration is the reduced size of the pixels themselves.

This study shows that modification of the hit position algorithm to include a weighted average does not significantly improve the impact parameter resolution. The effect of this modification could change for higher momentum incident particles, so additional simulations should be performed over a larger momentum range in order to explore the dependence of any improvements to impact parameter resolution on incident particle momentum. It has also been shown that the effect of the magnetic field on impact parameter resolution is negligible.

While the results in Figure 4.5 show that GEANT3's simulation of low energy electrons at the boundary between media does not agree with experimental results below incident electron energies of 1.0 MeV, the overall performance of GEANT3 in the tracking of electrons with kinetic energies of and above 1.0 MeV was satisfactory: the transmission and reflection coefficients calculated from the GEANT3 simulation closely matched experimental data for energies of and above 1.0 MeV. In order to verify the results, one could easily adapt the simplified pixel detector simulation to utilise GEANT4, which does not show the same deviation from experimental results for low energy electrons. GEANT3 was chosen for this investigation as it is the most commonly used transport package within the ALICE collaboration.

Additional investigations into the effect of energy leakage between pixels should be performed, by using a Gaussian smearing of hit positions, dependant on energy deposit size. This would certainly result in a degraded impact parameter resolution, but would provide a more realistic simulation of the effect of δ rays on impact parameter resolution. It would also allow for an investigation into the effect of modifying pixel properties, as the energy leakage would vary, depending on parameters of the individual pixels, such as size and material. Extending the simulation to include additional detectors would allow particles with higher momenta to be investigated, as the ITS uses the drift and strip detectors to calculate impact parameters for particles with momenta above 2 GeV/c.

An investigation into the efficiency of differentiating between primary and secondary vertices, with and without the production of δ rays, should be performed. For this task, the event generation package PYTHIA could be used, in order to

generate statistically representative primary particles of various types. This could be incorporated into the simulation constructed for this study using the Virtual Monte Carlo framework.

Appendix A

Common Variables and Quantities in High Energy Physics

A.1 Kinematic Variables

The variables used to describe the kinematics of heavy ion collisions are chosen either for their properties under Lorentz transformations or for the ease with which they can be measured experimentally. The **rapidity** of a particle is defined as

$$y = \frac{1}{2} \ln \left(\frac{E + p_z}{E - p_z} \right), \tag{A.1}$$

where E is the particle energy and p_z is the particle momentum along the beam axis (generally chosen as the z-axis). The transverse momentum $\mathbf{p_T} = \mathbf{p} - p_z \hat{\mathbf{z}}$ is invariant under Lorentz transformations along the z-axis. For particles with momentum purely in the z-direction (i.e $\mathbf{p_T} = \mathbf{0}$ and $|\mathbf{p}| = p_z$), the energy can be written as

$$E = m \cosh y, \tag{A.2}$$

while the momentum is given by

$$|\mathbf{p}| = m \sinh y. \tag{A.3}$$

For particles with $\mathbf{p_T} \neq \mathbf{0}$, one can define a **transverse mass** $m_T = \sqrt{m^2 + \mathbf{p_T}^2}$ and the energy and z-axis momentum are then given by

$$E = m_T \cosh y, \tag{A.4}$$

$$p_z = m_T \sinh y. \tag{A.5}$$

Thus, the energy of a particle as well as forward momentum can be easily calculated from a measurement of rapidity. The most useful property of the rapidity variable is its behaviour under frame changes. Unlike the relativistic velocity, addition of rapidity is simple:

$$y = y' + y_{\text{frame}}, \tag{A.6}$$

where y' is the rapidity measured in the moving frame and y_{frame} is the rapidity of the moving frame. In collider experiments with symmetric participants, the centre of mass frame is at rest with respect to the lab frame. Particles with high positive or negative rapidity correspond to those with a low polar angle θ to the beam axis, while particles with rapidity close to zero (known as mid-rapidity particles) have trajectories close to perpendicular to the beam axis, or $\theta \approx 90°$. This is shown in Figure A.1.

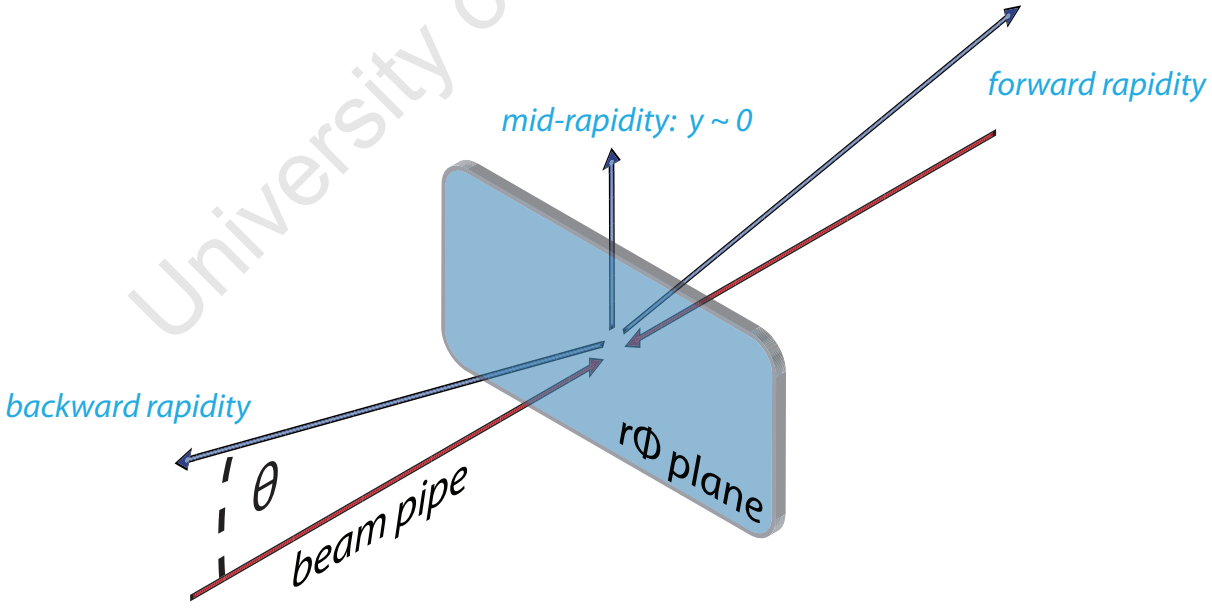

FIGURE A.1: Regions of high rapidity correspond to extremal polar angles, while mid-rapidity regions are perpendicular to the beam axis.

At ultra-relativistic energies, where $E \approx |\mathbf{p}|$, one can approximate the rapidity

by the **pseudo-rapidity** η, defined as

$$\eta = \frac{1}{2}\ln\frac{(|\mathbf{p}| + p_z)}{(|\mathbf{p}| - p_z)} \tag{A.7}$$

$$= \frac{1}{2}\ln\frac{(|\mathbf{p}| + |\mathbf{p}|\cos\theta)}{(|\mathbf{p}| - |\mathbf{p}|\cos\theta)} \tag{A.8}$$

$$= -\ln(\tan\frac{\theta}{2}). \tag{A.9}$$

Thus the pseudo-rapidity, and hence an estimate of the rapidity, can be measured by simply measuring the polar angle of outgoing particles.

A.2 Measured Quantities

Multiplicity

An important measurement in any experiment is the particle **multiplicity**: the number of detected particles in a given variable range. The charged particle multiplicity pseudo-rapidity distribution $\frac{dN_{\mathrm{ch}}}{d\eta}$ is a very simple result to measure in most circumstances.

Collision Centrality

In heavy ion collisions, it is unlikely that the two participants will collide with their centres exactly aligned. Instead, they will be offset by a certain **collision impact parameter**, b, which gives a measure of the **centrality** of the collision. Perfectly central collisions will have $b = 0$, while peripheral collisions can have values up to $b = R_a + R_b$, where R_a and R_b are the radii of the participants. While it is impossible to measure b directly, one can obtain information on the centrality of a collision by measuring the number of spectator nucleons[1] using detectors placed in the extremely forward pseudo-rapidity region. From this one can bin events into categories of centrality such as the most central 5% of measured collisions. Thus, without measuring the geometry of the collision itself, one can still obtain information on how particle yields vary with centrality.

[1] nucleons which do not take part in the collision

Nuclear Modification Factor

One of the most important aspects of heavy ion collisions is the comparison of yields between proton-proton collisions and nucleus-nucleus collisions. Many phenomena are expected to scale either with the number of participants or with the number of possible binary collisions. These predictions can be measured with the **nuclear modification factor**

$$R_{AA} = \frac{dN_{\mathrm{AA}}/dz}{N_{\mathrm{s}} dN_{\mathrm{pp}}/dz}, \tag{A.10}$$

where dN_{AA}/dz is the multiplicity distribution, as a function of chosen variable z, for nucleus-nucleus collisions, dN_{pp}/dz is the multiplicity distribution for proton-proton collisions and N_{s} is the scaling factor, normally $2A$ for processes that scale with the number of participants or A^2 for those that scale with the number of binary collisions in a most central event. A value of $R_{AA} = 1$ implies that there is no nuclear effect.

Elliptic Flow Coefficient v_2

The azimuthal distribution of particle spectra $\frac{d^2N}{d\phi dp_T}$ can be expanded to a Fourier series as

$$\frac{d^2N}{d\phi dp_T} = N_0(1 + v_1\cos(\phi) + 2v_2\cos(2\phi) + ...). \tag{A.11}$$

The second coefficient v_2 is the **elliptic flow** and measures the anisotropy of the azimuthal angle distribution. It can be shown to be equivalently defined as [37]:

$$v_2 = \left\langle \frac{p_x^2 - p_y^2}{p_x^2 + p_y^2} \right\rangle. \tag{A.12}$$

Track Impact Parameter

Of vital importance to the detection of heavy quark decays is the **track impact parameter** d_0, defined as the distance of shortest approach from a track to the primary vertex, as shown in Figure A.2.

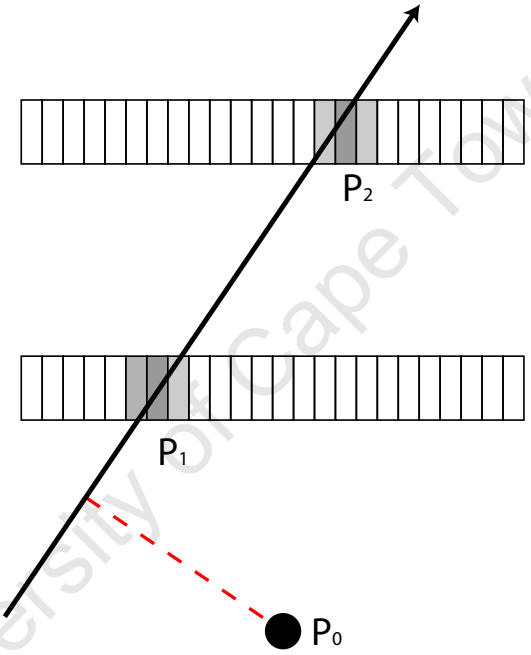

FIGURE A.2: The impact parameter d_0 is shown as the dashed line, perpendicular to the extension of the line drawn from $\mathbf{P_2}$ to $\mathbf{P_1}$, where $\mathbf{P_2}$ and $\mathbf{P_1}$ are track hits on a pixel detector.

Bibliography

[1] I. Arsene et al. Quark Gluon Plasma and Color Glass Condensate at RHIC? The perspective from the BRAHMS experiment. *Nuclear Physics A*, 757, 2005.

[2] K. Nakamura et al. Review of Particle Physics. *Journal of Physics G: Nuclear and Particle Physics*, 37, 2010.

[3] P. Braun-Munzinger, J. Stachel, and C. Wetterich. Chemical freeze-out and the QCD phase transition temperature. *Physics Letters B*, 596(1-2):61–69, 2004. ISSN 0370-2693.

[4] T. Matsui and H. Satz. J/ψ suppression by quark-gluon plasma formation. *Physics Letters B*, 178(4):416–422, 1986.

[5] F. Karsch. The phase transition to the quark gluon plasma: Recent results from lattice calculations. *Nuclear Physics, Section A*, 590(1-2):367–381, 1995.

[6] J Cleymans et al. Hadron production in ultra-relativistic nuclear collisions: Quarkyonic matter and a triple point in the phase diagram of QCD. *Nuclear Physics A*, 2010.

[7] K. Nakamura et al. High-energy Collider Parameters. *Journal of Physics G: Nuclear and Particle Physics*, 37, 2010.

[8] B. Müller. Physics of the quark-gluon plasma. *Arxiv preprint nucl-th/9211010*, 1992.

[9] B. Donigus. Ultra-relativistic nuclear collisions and production of hot fireballs at SPS/RHIC. In *Ultra-relativistic nuclear collisions and Production of Hot Fireballs at SPS/RHIC*, page 5. Presented at RI Seminars 2010, Paris, 2009.

[10] N. S. Craigie, H. F. Jones, and P. Milani. Study of charm production through $e\mu$ and ek correlations. *Phys. Rev. D*, 19(3):897–921, Feb 1979.

[11] MJ Tannenbaum. Measurements of Hard-Scattering by PHENIX at RHIC. *Nuclear Physics B (Proceedings Supplements)*, 177:150–155, 2008.

[12] J. Adams et al. Experimental and theoretical challenges in the search for the quark gluon plasma: The STAR collaboration's critical assessment of the evidence from RHIC collisions. *Nuclear Physics A*, 757:102–183, 2005.

[13] BB Back et al. Nuclear Experiment Title: The PHOBOS Perspective on Discoveries at RHIC. *Nuclear Physics A*, 757:101, 2005.

[14] G.M. Garcia. ALICE potential for heavy-flavour physics. *Journal of Physics G: Nuclear and Particle Physics*, 34:S943–S946, 2007.

[15] A. Dainese. Charm production and in-medium QCD energy loss in nucleus-nucleus collisions with ALICE. A performance study. *Arxiv preprint nucl-ex/0311004*, 2003.

[16] D. Manglunki et al. Ions for LHC: status of the injector chain. *Proc. APAC07, Indore, India*, 2007.

[17] TRD Alice. TRD Technical Design Report. *CERN/LHCC*, 21, 2001.

[18] B. Alessandro et al. ALICE: Physics performance report, volume II. *Journal of Physics G: Nuclear and Particle Physics*, 32:1295–2040, 2006.

[19] K. Aamodt et al. The ALICE experiment at the CERN LHC. *J. Instrum.*, 3, 2008.

[20] P Cortese. *ALICE transition-radiation detector: Technical Design Report*. Technical Design Report ALICE. CERN, Geneva, 2001.

[21] P Cortese. *ALICE Time-Of Flight system (TOF): addendum to the Technical Design Report*. Technical Design Report ALICE. CERN, Geneva, 2002.

[22] V Man'ko et al. *ALICE Photon Spectrometer (PHOS): Technical Design Report*. Technical Design Report ALICE. CERN, Geneva, 1999.

[23] ITS Alice. ITS Technical Design Report. *CERN/LHCC*, 21, 1999.

[24] L. Rossi, P. Fischer, and T. Rohe. *Pixel detectors: From fundamentals to applications*. Springer Verlag, 2006.

[25] Lund University. Pythia. `http://home.thep.lu.se/~torbjorn/Pythia.html`.

[26] The ROOT Team. ROOT data analysis framework. `http://root.cern.ch`.

[27] I. Hrivnacova. Virtual Monte Carlo. `http://root.cern.ch/drupal/content/vmc`.

[28] F. Carminati et al. GEANT Users Guide. *CERN program Library*, 1993.

[29] B. Rossi. *High-energy particles*. Prentice-Hall, 1965.

[30] K. Nakamura et al. Passage of particles through matter. *Journal of Physics G: Nuclear and Particle Physics*, 37, 2010.

[31] H. A. Bethe. Molière's theory of multiple scattering. *Phys. Rev.*, 89(6):1256–1266, Mar 1953.

[32] SM Seltzer and MJ Berger. Transmission and reflection of electrons by foils. *Nucl. Instrum. Methods, v. 119, no. 1, pp. 157-176*, 1974.

[33] M. Maire. Electromagnetic Interactions of Particles with Matter. *Molecular Imaging: Computer Reconstruction and Practice*, pages 39–72, 2008.

[34] Sebastien Incerti. Geant4 Low Energy Electromagnetic Physics Working Group. `https://twiki.cern.ch/twiki/bin/view/Geant4/LowEnergyElectromagneticPhysicsWorkingGroup`.

[35] G.E Bruno et al. Tuning of the SPD simulation model in AliRoot. *ALICE Internal Note*, 2008.

[36] K. Safarik. ALICE at ICHEP. page 25. Presented at ICHEP 2010, Paris, 2010.

[37] K. Dusling and D. Teaney. Simulating elliptic flow with viscous hydrodynamics. *Phys. Rev. C*, 77:034905, 2008.